4-4-2018

A radiative transfer framework for non-exponential media

Benedikt Bitterli
Dartmouth College

Srinath Ravichandran
Dartmouth College

Thomas Müller
Disney Research

Magnus Wrenninge
Pixar Animation Studios

Jan Novák
Disney Research

See next page for additional authors

A radiative transfer framework for non-exponential media

Dartmouth Computer Science Technical Report TR2018-841, Revision 1 (April 4th, 2018)

BENEDIKT BITTERLI, Dartmouth College
SRINATH RAVICHANDRAN, Dartmouth College
THOMAS MÜLLER, Disney Research
MAGNUS WRENNINGE, Pixar Animation Studios
JAN NOVÁK, Disney Research
STEVE MARSCHNER, Cornell University
WOJCIECH JAROSZ, Dartmouth College

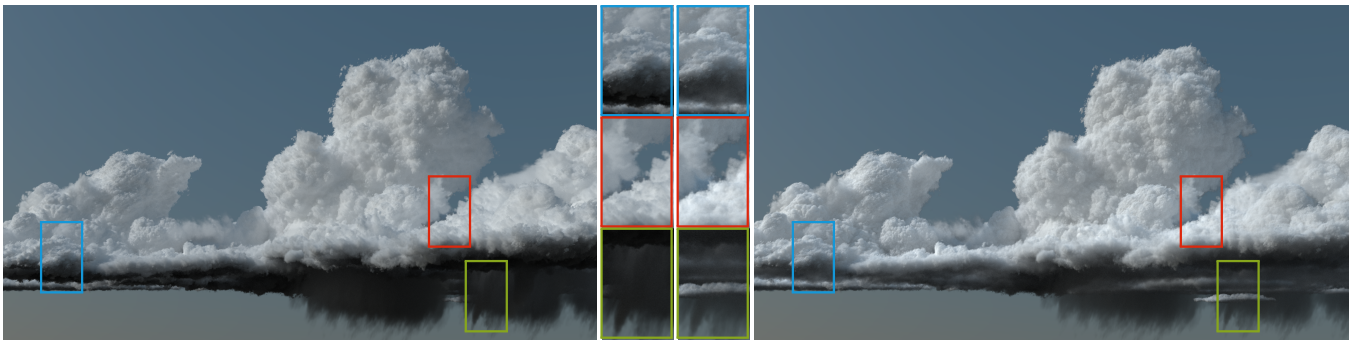

Fig. 1. We show a cloud rendered with a traditional exponential transmittance (left) and with a non-exponential, long-tailed transmittance curve (right). The non-exponential transmittance leads to both deeper light penetration as well as a denser appearance near the surface, allowing for a richer appearance.

We develop a new theory of volumetric light transport for media with non-exponential free-flight distributions. Recent insights from atmospheric sciences and neutron transport demonstrate that such distributions arise in the presence of correlated scatterers, which are naturally produced by processes such as cloud condensation and fractal-pattern formation. Our theory accommodates correlations by disentangling the concepts of the free-flight distribution and transmittance, which are equivalent when scatterers are statistically independent, but become distinct when correlations are present. Our theory results in a generalized path integral which allows us to handle non-exponential media using the full range of Monte Carlo rendering algorithms while enriching the range of achievable appearance. We propose parametric models for controlling the statistical correlations by leveraging work on stochastic processes, and we develop a method to combine such unresolved correlations (and the resulting non-exponential free-flight behavior) with explicitly modeled macroscopic heterogeneity. This provides a powerful authoring approach where artists can freely design the shape of the attenuation profile separately from the macroscopic heterogeneous density, while our theory provides a physically consistent interpretation in terms of a path space integral. We address important considerations for graphics including energy conservation, reciprocity, and bidirectional rendering algorithms, all in the presence of surfaces and correlated media.

CCS Concepts: • **Computing methodologies** → **Ray tracing**;

Additional Key Words and Phrases: Computer Graphics

1 INTRODUCTION

Standard techniques in graphics for rendering scenes containing participating media rely on the classical radiative transfer equation (RTE) [Chandrasekhar 1960]. A central assumption of the classical RTE is that the medium is composed of tiny, *statistically independent* scatterers. This independence leads to a "memoryless" Poisson process and the familiar exponential falloff of light (see Figure 2a). While this model has proved useful in a wide range of applications, it does not accurately describe media where there are any kind of correlations between individual scatterers, including unresolved small-scale fluctuations in density.

1.1 The case for correlated/non-exponential transport

Growing evidence from atmospheric sciences shows that clouds have correlations in the positions of water droplets at scales ranging at least from centimeters to kilometers [Davis et al. 1999; Kostinski and Jameson 2000]. If significant correlations exist on the scale of the mean-free path of the medium [Davis and Marshak 2004], non-exponential free-flight distributions arise, where positive [Borovoi 2002; Kostinski 2001] and negative [Shaw et al. 2002] correlations lead to slower-than-exponential and faster-than-exponential free-flight, respectively.

In Figure 2 we perform a simple Monte Carlo experiment where we trace random photons through 2D media consisting of explicitly modeled absorbing particles. We gather statistics about the averaged transmittance (e) by tabulating along the horizontal axis the fraction of photons that survive for a given distance. In each case the average number of particles is identical, and it is the statistical correlations that give rise to different light attenuation behavior. Intuitively, particles in positively correlated media (c,d) "clump" together and leave larger gaps than expected, so photons that traverse these gaps

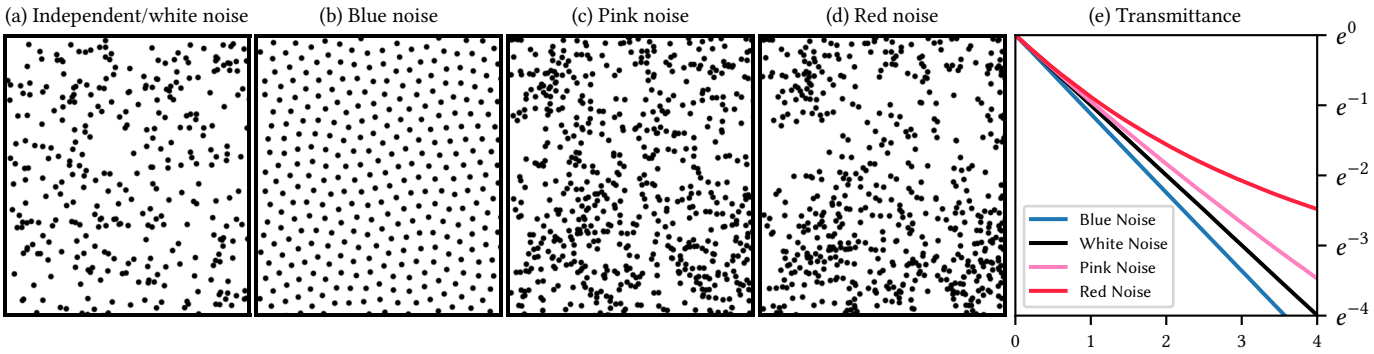

Fig. 2. We show media with discrete scatterers of different distributions (a)–(d), and the average transmittance measured in these media as a function of mean free paths (e). Independently placed scatterers ((a), white noise) lead to the classical exponential transmittance. Negatively correlated scatterers ((b), blue noise) lead to faster-than-exponential extinction. Positively correlated scatterers ((c)–(d), pink/red noise) lead to slower-than-exponential extinction.

skew the free-flight distribution towards the tail, allowing light to penetrate further on average. The opposite happens in negatively correlated media. Ignoring these correlations and instead assuming statistical independence leads to an inaccurate estimation of light transport with notably different visual appearance; c.f. Figure 1.

We wish to account for such violations of independence in a physically plausible manner, and enable practical rendering algorithms that enrich the level of control over the appearance of participating media. We first show (Section 2) that the simplest approach of replacing transmittance in the classical RTE with anything other than an exponential inevitably violates energy conservation. We therefore (Section 3) revisit the RTE, removing the exponential assumption, and derive a generalized RTE that allows arbitrary free-flight PDFs while conserving energy. Our derivations reveal that the notions of free-flight PDF and transmittance, which happen to be the same in the classical RTE, need to be kept distinct in the non-exponential case, requiring path segments ending on surfaces and in volumes to be treated differently. Our theory results in a generalized path integral which shows how to easily change any Monte Carlo path-sampling algorithm to accommodate arbitrary free-flight distributions. To leverage this new flexibility, we use the mathematical formalisms of stochastic Gaussian processes and fractal noise [Barnsley et al. 1988] to obtain artist-directable parametric models for non-exponential free-flight distributions (Section 4), and we develop a procedural way to superimpose the resulting distributions on explicitly modeled heterogeneous media (Section 5). This results in a more flexible and directable system where artists can author classical media properties but additionally choose between different free-flight distributions, all while providing a consistent interpretation of the light transport that is independent of the chosen Monte Carlo rendering algorithm.

1.2 Related work

Atmospheric sciences & neutron transport. Motivated by empirical observations [Davis et al. 1999; Kostinski and Jameson 2000] of multi-scale correlations of liquid water content in clouds, the atmospheric science community has developed many statistical models [Borovoi 2002; Davis and Marshak 2004; Davis and Mineev-Weinstein 2011; Davis and Xu 2014; Kostinski 2001; Shaw et al. 2002] to explain how such correlations lead to non-exponential aggregate transport behavior. These methods typically reduce the cloud to a fully homogenized slab while introducing statistically equivalent non-exponential free-flights. We adopt the fractal variability model proposed by Davis and colleagues [2011; 2014], but additional provide a way to superimpose the non-exponentiality from such unresolved fluctuations onto resolved macro-scale heterogeneity. Likewise, motivated by correlations and non-uniformity of pebble-bed reactors, Larsen and Vasquez [2011; 2014a; 2014b] recently derived generalized RTE-like models for neutron transport that allows non-exponential, angular-dependent free flight distributions by introducing an additional "memory" parameter tracking the distance since the last interaction. Non-exponential behavior also arises when there is "cross-talk" between neutrons (photons) of different energy-levels (wavelengths). This is often ignored in graphics – unless fluorescence/in-elastic scattering [Gutierrez et al. 2008; Jarabo and Arellano 2018] needs to be considered – but is quite common in neutron transport where multi-energy simulations are standard practice. D'Eon [2016] provides an excellent overview of previous work on non-exponential free-flights outside of graphics. Unfortunately, it is difficult to directly leverage these prior formulations in graphics, since they do not construct a theory considering both volumes and "solid" surfaces that can readily be solved using a chosen Monte Carlo rendering algorithm.

Graphics. There has also been some work in graphics that explored non-classical transport, often in the context of approximating complex geometry as a continuous participating medium. Moon et al. [2007] introduced the concept of non-exponential transport to graphics, and several approaches [Meng et al. 2015; Moon et al. 2008; Müller et al. 2016] have since considered the problem of accelerating multiple scattering within discrete random (granular) media. These methods all addressed isolated rendering problems (via data-driven tabulation or by simplifying to the classical RTE) and do not provide a theory for how to handle non-classical transport in general. Jakob et al. [2010] and follow-up work [Dupuy et al. 2016; Heitz et al. 2015] took a step in this direction by enhancing the classical RTE to account for angular structure/correlations using the microflake model. These theories, however, still ignore the *spatial* correlations that give rise to non-exponential free-flight behavior in media. Our

theory shows how to achieve this by modeling unresolved spatial correlations and density fluctuations (volumetric "roughness") statistically, akin to how microfacet models [Blinn 1977; Cook and Torrance 1981] represent surface roughness statistically.

Artistic control. The film industry has recently started exploring the use of non-exponential behavior for artistic control and accelerated multiple scattering [Bouthors et al. 2008; Nowrouzezahrai et al. 2011; Wrenninge et al. 2013, 2011]. Common strategies include artificially lengthening the mean-free path for shadow rays of higher-order scattering [Bouthors et al. 2008; Wrenninge et al. 2011] or replacing exponential transmittance with a sum of exponentials [Wrenninge et al. 2013]. While originally developed in an ad-hoc way, we discuss in Section 4 how such sums of exponentials have a physically grounded interpretation. Pixar's RenderMan likewise allows specifying separate "shallow" and "deep" scattering mean-free paths to preserve fine-scale surface details while controlling long-range subsurface scattering. D'Eon [2013] derived diffusion equations for non-exponential free-flights which could conceivably be used in this context. Most recently, Wrenninge et al. [2017] applied non-exponential free-flights from Davis and Xu [2014] to homogeneous path-traced subsurface scattering. While such artistic techniques have proven useful in production, the industry has gradually shifted to physically based light transport using path tracing-based approaches [Christensen and Jarosz 2016; Fong et al. 2017; Keller et al. 2015], reinforcing the need for a more flexible theory of light transport in scenes with surfaces and correlated heterogeneous media which can be solved in a consistent way using any desired Monte Carlo rendering algorithm.

2 NON-EXPONENTIALITY IS NON-TRIVIAL

It is not immediately obvious why rendering with non-exponential transmittance requires a new theory—it seems trivial to modify the classical RTE and substitute an arbitrary, monotonically decreasing function for the transmittance. In this section, we will therefore first demonstrate in a simple hypothetical example why such an approach will inherently violate energy conservation. This motivates our derivation of a new generalization of the RTE that conserves energy even with non-exponential transmittance, which we present in Section 3.

In the following, we consider a scene filled with a participating medium characterized by its extinction coefficient $\sigma_t(\mathbf{x})$ and albedo $\alpha(\mathbf{x})$, where $\sigma_s = \sigma_t \cdot \alpha$ is the scattering coefficient. We consider a pencil beam of light starting at $\mathbf{x}$ traveling in direction $\boldsymbol{\omega}$. The beam intersects a surface at point $\mathbf{x}_z$, and we use the convention $\mathbf{x}_s = \mathbf{x} + s \cdot \boldsymbol{\omega}$ to denote points along the beam.

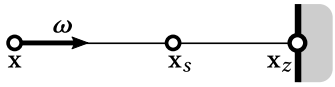

The radiance L received by points on the beam decreases with distance as a result of extinction by the medium. The rate of decrease is determined by the extinction coefficient, with the relationship

$$\frac{\mathrm{d}}{\mathrm{d}s} L(\mathbf{x}_s, \boldsymbol{\omega}) = -\sigma_t(\mathbf{x}_s) L(\mathbf{x}_s, \boldsymbol{\omega}), \tag{1}$$

which forms the cornerstone of the classical RTE [Chandrasekhar 1960]. In words, the differential equation states that at every infinitesimal step ds, a fraction of the radiance (defined by $\sigma_t(\mathbf{x})$) is absorbed. The solution to the above equation is the Beer-Lambert law, which is obtained through integration:

$$L(\mathbf{x}_s) = L_0(\mathbf{x}, \boldsymbol{\omega})\, \mathrm{e}^{-\int_0^s \sigma_t(\mathbf{x}_t)\,\mathrm{d}t}, \tag{2}$$

where L_0 is the radiance at the start of the beam. The factor on the right defines *transmittance* Tr in terms of the *optical depth* τ

$$\mathrm{Tr}(\tau) = \mathrm{e}^{-\tau}, \quad \text{and} \quad \tau(\mathbf{x}, \mathbf{x}_s) = \int_0^s \sigma_t(\mathbf{x}_t)\,\mathrm{d}t. \tag{3}$$

This classical definition of transmittance is a fundamental consequence of starting with the differential form (1), which assumes the total extinction arises due to a sequence of infinitesimal, *independent* extinction events. At a high level, $\mathrm{Tr}(\tau)$ describes the fraction of light that is transmitted through τ units of medium; however, the definition above is much more restrictive, and can only ever permit exponential transmittance.

Even so, it appears trivial to introduce non-exponentiality at the integral level (2) simply by substituting a function other than an exponential for $\mathrm{Tr}(\tau)$. However, we will now show that this inherently leads to non-physicality.

Consider the radiance at the start of the beam. Its energy must be distributed between two terms: the amount of light that scatters in the medium, and the remaining fraction that reaches the surface. Assuming a non-absorptive medium ($\alpha = 1$), the sum of both terms must equal $L_0(\mathbf{x}, \boldsymbol{\omega})$—otherwise, energy is either lost or gained along the way. This results in the following constraint:

$$L_0(\mathbf{x}, \boldsymbol{\omega}) = L_0(\mathbf{x}, \boldsymbol{\omega})\mathrm{Tr}(\mathbf{x}, \mathbf{x}_z) + \int_0^z L_0(\mathbf{x}, \boldsymbol{\omega})\mathrm{Tr}(\mathbf{x}, \mathbf{x}_s)\sigma_s(\mathbf{x})\,\mathrm{d}s, \tag{4}$$

where we have used $\mathrm{Tr}(\mathbf{x}, \mathbf{x}_s) = \mathrm{Tr}(\tau(\mathbf{x}, \mathbf{x}_s))$. The above equation can be simplified by dividing out $L_0(\mathbf{x}, \boldsymbol{\omega})$:

$$1 = \mathrm{Tr}(\mathbf{x}, \mathbf{x}_z) + \int_0^z \mathrm{Tr}(\mathbf{x}, \mathbf{x}_s)\sigma_s(\mathbf{x})\,\mathrm{d}s. \tag{5}$$

Using the fact that $\mathrm{d}\tau/\mathrm{d}s = \sigma_t(\mathbf{x}_s)$, and $\sigma_t = \sigma_s$ when $\alpha = 1$, we can perform a change of variable from ds to dτ to obtain

$$1 = \mathrm{Tr}(\tau(\mathbf{x}, \mathbf{x}_z)) + \int_0^{\tau(\mathbf{x}, \mathbf{x}_z)} \mathrm{Tr}(\tau)\,\mathrm{d}\tau\,. \tag{6}$$

Any transmittance function Tr that does not satisfy the above constraint violates energy conservation and must inevitably lead to energy loss or energy gain when inserted into the classical RTE.

Equation (6) is an ordinary differential equation of the form $1 = f'(x) + f(x) - f(0)$. The only solutions that satisfy it are expressed by $\mathrm{Tr}(\tau) = c \cdot \mathrm{e}^{-\tau}$. In other words, *only an exponential transmittance* satisfies energy conservation in the classical RTE. Violation of energy conservation is not only a practical problem, but also means that the underlying process is non-physical. This suggests that a non-exponential transmittance is simply not possible in a physically consistent framework.

However, we will show in the next section that the classical RTE uses $\mathrm{Tr}(\tau)$ to express two distinct concepts: the transmittance and the free-flight PDF. When $\mathrm{Tr}(\tau)$ is an exponential, these two quantities happen to be identical; however, failing to separate these two ideas leads to violations of energy conservation when we attempt to introduce non-exponentiality. To resolve these issues, we derive a generalized theory of volumetric light transport that makes the

free-flight PDF a first-class citizen, and defines the transmittance in terms of free-flight probabilities.

3 NON-EXPONENTIAL RADIATIVE TRANSPORT

Our goal is to derive a new theory that permits physically plausible simulation with non-exponential transmittance functions. In order for this new theory to be useful, it should possess the following properties:

- Non-exponential transmittance should be supported from the ground up, rather than introduced after the fact.
- The theory should be fully energy conserving, such that in the absence of absorption, no energy is lost or gained.
- For an exponential transmittance, the theory should reduce to the classical light transport framework.

This ensures that the new theory solves the problems demonstrated in the previous section, while remaining backwards-compatible with the traditional light transport framework.

One property of our theory is that it is not reciprocal for non-exponential media. This is not a major practical concern, but it is interesting from a theoretical standpoint, and we discuss details of this fact in Section 3.8.

3.1 Basic Definitions

The focus of our new theory is on energy conservation. This motivates us to reason about light transport from an *analog* perspective, in which we track the physical photons that are scattered and transported within the medium. We begin our derivation by formulating balance equations for the transport and scattering of photons that ensure that photons do not get destroyed or created during transport. This allows us to ultimately derive a new energy conserving path integral for non-exponential transport.

Our theory will use non-exponential transmittance to represent detail beyond what is resolved in the macroscopic properties of the medium. Since the classical media properties—such as the extinction coefficient σ_t and optical depth τ—are already familiar and present in current rendering systems, we will use them as scaffolding upon which we build our theory. Once non-exponential transmittance is introduced, however, these quantities no longer have the prior physical interpretations, since they describe the medium as if no hidden correlations were present.

In our framework, we consider the free-flight PDF $p_\tau(\tau)$ of photons a fundamental property of the medium, and we define it with respect to the macroscopic optical depth τ. This function represents the probability density that a photon enters a collision with the medium after passing through an optical depth of τ. We place no restrictions on the free-flight PDF, other than it being a proper PDF; that is

$$\int_0^\infty p_\tau(\tau)\,\mathrm{d}\tau = 1 \quad \text{and} \quad p_\tau(\tau) \geq 0\,. \tag{7}$$

For an exponential medium, the free-flight PDF corresponds to $p_\tau^{\exp}(\tau) = e^{-\tau}$. It is important to note that $p_\tau(\tau)$ is a physical property of the medium; it is distinct from the concept of a distance-sampling PDF in Monte Carlo rendering, which only influences the efficiency of the algorithm.

Frequently, we need to express the free-flight PDF in units of distance, rather than optical depth. This incurs a multiplication by a Jacobian, and we obtain

$$p_s(\mathbf{x}, \mathbf{x}_s) = p_\tau(\tau(\mathbf{x}, \mathbf{x}_s))\frac{\mathrm{d}\tau}{\mathrm{d}s} = p_\tau(\tau(\mathbf{x}, \mathbf{x}_s))\sigma_t(\mathbf{x}_s)\,. \tag{8}$$

Using photons as a basic building block, we can describe transport in the medium using densities of photon events. Of particular interest are two densities: $L_i(\mathbf{x}, \boldsymbol{\omega})$, the density of photons arriving from $\boldsymbol{\omega}$ entering a collision at $\mathbf{x}$; and $L_o(\mathbf{x}, \boldsymbol{\omega})$, the density of photons departing a collision at $\mathbf{x}$ in direction $\boldsymbol{\omega}$. We will also make use of $L_e(\mathbf{x}, \boldsymbol{\omega})$, the density of photons emitted at $\mathbf{x}$ toward $\boldsymbol{\omega}$.

By reasoning about the exchange of departing and arriving photons, we can derive a set of balance equations that link the two densities. The densities have different form depending on whether the interacting point is on a surface or in a medium. We decorate quantities with a superscript to specify which density is referenced; for example, L_i^m is the density of photons incident on a medium point, and L_i^s the density on a surface point. When no superscript is given, $L_i(\mathbf{x}, \boldsymbol{\omega})$ is understood to be equal to $L_i^s(\mathbf{x}, \boldsymbol{\omega})$ if $\mathbf{x}$ lies on a surface, and L_i^m otherwise. The same notation applies to L_o and L_e.

3.2 Transport

Transport relates the density of incident photons (L_i) to the density of departing photons (L_o). A photon that leaves an interaction at $\mathbf{x}_s$ toward direction $\boldsymbol{\omega}$ travels some distance through the medium before entering another interaction at $\mathbf{x}$. The probability density of this interaction is a function of the distance between $\mathbf{x}_s$ and $\mathbf{x}$.

If $\mathbf{x}$ lies in the medium, then we have already defined this probability density: It is $p_s(\mathbf{x}_s, \mathbf{x})$, the free-flight PDF. If $\mathbf{x}$ lies on a surface, the interaction probability can be obtained from the fact that *all* photons encountering a surface must interact with it, unless they collide with the medium on the way there; i.e. it is the probability of not interacting with the medium:

$$\mathrm{Tr}(\mathbf{x}_z, \mathbf{x}) = 1 - \int_0^z p_s(\mathbf{x}_s, \mathbf{x})\,\mathrm{d}s. \tag{9}$$

This quantity is precisely the transmittance! It is the probability of interacting with the surface, or the fraction of photons transmitted through z units of medium.

Knowing the interaction probabilities, we obtain the total incident density at $\mathbf{x}$ by integrating the product of interaction probability and exitant density L_o over all potential source locations. Occlusion only allows photons departing locations between $\mathbf{x}$ and the nearest surface point $\mathbf{x}_z$ along the ray $(\mathbf{x}, \boldsymbol{\omega})$ to contribute (see figure below).

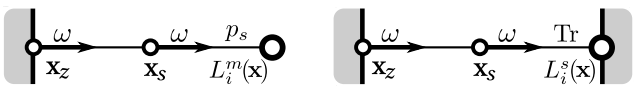

Assembling these facts yields the transport equations:

$$L_i^m(\mathbf{x}, \boldsymbol{\omega}) = p_s(\mathbf{x}_z, \mathbf{x})L_o^s(\mathbf{x}_z, -\boldsymbol{\omega}) + \int_0^z p_s(\mathbf{x}_s, \mathbf{x})L_o^m(\mathbf{x}_s, -\boldsymbol{\omega})\,\mathrm{d}s, \tag{10}$$

$$L_i^s(\mathbf{x}, \boldsymbol{\omega}) = \mathrm{Tr}(\mathbf{x}_z, \mathbf{x})L_o^s(\mathbf{x}_z, -\boldsymbol{\omega}) + \int_0^z \mathrm{Tr}(\mathbf{x}_s, \mathbf{x})L_o^m(\mathbf{x}_s, -\boldsymbol{\omega})\,\mathrm{d}s. \tag{11}$$

Discussion. In contrast to Equation (3), Equation (9) defines the transmittance in terms of p_s instead of a differential equation. To aid analysis, we rewrite the transmittance in terms of τ:

$$\mathrm{Tr}(\tau) = 1 - \int_0^\tau p_\tau(\tau')\,\mathrm{d}\tau' = \int_\tau^\infty p_\tau(\tau')\,\mathrm{d}\tau' \tag{12}$$

This constrains the transmittance to be an integral of a PDF. A transmittance defined this way has several desirable properties: It is non-negative and monotonically decreasing, it returns a transmittance of 1 for $\tau = 0$ and it tends to zero as τ tends to infinity. Crucially, if we insert the exponential free-flight PDF $p_\tau^{\exp}(\tau)$, we obtain the transmittance

$$\mathrm{Tr}(\tau) = \int_\tau^\infty e^{-\tau'}\,\mathrm{d}\tau' = e^{-\tau} = p_\tau^{\exp}(\tau). \tag{13}$$

That is, the transmittance and the free-flight PDF are identical in the exponential case. This is why the classical RTE does not distinguish between the two concepts. As a consequence, the incident density on surfaces and media is identical in the classical RTE, whereas we have explicitly separated the two ((10) and (11)). As we will show later, this allows our theory to achieve full energy conservation for any free-flight PDF.

3.3 Scattering

Scattering in our framework proceeds identically to the classical RTE, but we briefly derive it here for completeness. The density of photons departing a point $\mathbf{x}$ consists of two terms: Particles that were emitted at $\mathbf{x}$, and photons that arrived from elsewhere and scattered at $\mathbf{x}$. If $\mathbf{x}$ lies in the medium, the density of interacting photons is already known: It is $L_i^m(\mathbf{x}, \boldsymbol{\omega}')$, for any direction $\boldsymbol{\omega}'$. Of those photons, only the fraction $\alpha(\mathbf{x})$ is being scattered, and the phase function $\rho^m(\mathbf{x}, \boldsymbol{\omega}, \boldsymbol{\omega}')$ describes the directional scattering density for any direction $\boldsymbol{\omega}$. Integrating over all incident directions then gives the density of scattered photons.

We obtain the emission term from the product of the self-emission L_e and the density σ_t of the self-emitting medium. Adding emitted and scattered densities yields

$$L_o^m(\mathbf{x}, \boldsymbol{\omega}) = \sigma_t(\mathbf{x}) L_e^m(\mathbf{x}, \boldsymbol{\omega}) + \int_{S^2} \rho^m(\mathbf{x}, \boldsymbol{\omega}', \boldsymbol{\omega}) L_i^m(\mathbf{x}, \boldsymbol{\omega}') \alpha(\mathbf{x})\,\mathrm{d}\boldsymbol{\omega}'. \tag{14}$$

The surface case follows from identical reasoning, only that we replace albedo and phase function with the BRDF ρ^s and foreshortening factor:

$$L_o^s(\mathbf{x}, \boldsymbol{\omega}) = L_e^s(\mathbf{x}, \boldsymbol{\omega}) + \int_{S^2} \rho^s(\mathbf{x}, \boldsymbol{\omega}', \boldsymbol{\omega}) L_i^s(\mathbf{x}, \boldsymbol{\omega}') \cos\theta\,\mathrm{d}\boldsymbol{\omega}'. \tag{15}$$

Note that $\boldsymbol{\omega}'$ points toward $\mathbf{x}$ instead of away from $\mathbf{x}$ as in the standard definition of the BRDF.

3.4 Simplifications

Equations (10–15) fully describe the transport within the medium. We can see that Equation (10) and (11) are quite similar, and it makes sense to simplify them into a combined equation to make the rest of the derivation easier. Let $\mathcal{V}$ be the set of all volume points, and $\partial\mathcal{V}$ the set of all surface points. We then define the helper functions

$$E(\mathbf{x}', \mathbf{x}) = \begin{cases} \mathrm{Tr}(\mathbf{x}', \mathbf{x}) & \text{if } \mathbf{x} \in \partial\mathcal{V} \\ p_\tau(\tau(\mathbf{x}', \mathbf{x})) & \text{if } \mathbf{x} \in \mathcal{V} \end{cases} \tag{16}$$

$$\Sigma(\mathbf{x}) = \begin{cases} 1 & \text{if } \mathbf{x} \in \partial\mathcal{V} \\ \sigma_t(\mathbf{x}) & \text{if } \mathbf{x} \in \mathcal{V}, \end{cases} \tag{17}$$

where we call $E(\mathbf{x}', \mathbf{x})$ the *edge throughput*. This is an important term: It encapsulates the difference between our generalized theory and the classical RTE. Notably, when free-flights are exponential, $E(\mathbf{x}', \mathbf{x})$ reduces to $e^{-\tau(\mathbf{x}', \mathbf{x})}$ for both surfaces and media.

Of particular interest is the product $E(\mathbf{x}', \mathbf{x})\Sigma(\mathbf{x})$: It is equivalent to the transmittance $\mathrm{Tr}(\mathbf{x}', \mathbf{x})$ when $\mathbf{x}$ is on a surface, and equivalent to the free-flight PDF $p_s(\mathbf{x}', \mathbf{x})$ when $\mathbf{x}$ is in a medium. This product will show up frequently in equations, and we will refer to it as the *transport kernel*

$$T(\mathbf{x}', \mathbf{x}) = E(\mathbf{x}', \mathbf{x})\Sigma(\mathbf{x}) \tag{18}$$

with which we can obtain the combined equation

$$L_i(\mathbf{x}, \boldsymbol{\omega}) = T(\mathbf{x}_z, \mathbf{x}) L_o^s(\mathbf{x}_z, -\boldsymbol{\omega}) + \int_0^z T(\mathbf{x}_s, \mathbf{x}) L_o^m(\mathbf{x}_s, -\boldsymbol{\omega})\,\mathrm{d}s\,. \tag{19}$$

In a similar vein, we combine Equation (14) and (15) by introducing helper functions for scattering and foreshortening factor

$$\rho(\mathbf{x}, \boldsymbol{\omega}, \boldsymbol{\omega}') = \begin{cases} \rho^s(\mathbf{x}, \boldsymbol{\omega}, \boldsymbol{\omega}') & \text{if } \mathbf{x} \in \partial\mathcal{V} \\ \rho^m(\mathbf{x}, \boldsymbol{\omega}, \boldsymbol{\omega}')\alpha(\mathbf{x}) & \text{if } \mathbf{x} \in \mathcal{V} \end{cases} \tag{20}$$

$$D(\mathbf{x}, \boldsymbol{\omega}) = \begin{cases} |\boldsymbol{\omega} \cdot n(\mathbf{x})| & \text{if } \mathbf{x} \in \partial\mathcal{V} \\ 1 & \text{if } \mathbf{x} \in \mathcal{V} \end{cases} \tag{21}$$

to obtain

$$L_o(\mathbf{x}, \boldsymbol{\omega}) = \Sigma(\mathbf{x}) L_e(\mathbf{x}, \boldsymbol{\omega}) + \int_{S^2} \rho(\mathbf{x}, \boldsymbol{\omega}', \boldsymbol{\omega}) L_i(\mathbf{x}, \boldsymbol{\omega}') D(\mathbf{x}, \boldsymbol{\omega}')\,\mathrm{d}\boldsymbol{\omega}'. \tag{22}$$

These combined equations succinctly describe our theory. To complete this section, we now derive the full path integral, which permits in-depth analysis (Section 3.6–3.8) and practical rendering algorithms (Section 6).

3.5 Generalized Path Integral

The path integral is a concise way of expressing measurements of photon events. We use $W(\mathbf{x}, \boldsymbol{\omega})$ to denote the measurement response of a (surface or volume) sensor. The measurement I taken by this sensor is

$$I = \int_{\mathcal{M}} \int_{S^2} W(\mathbf{x}, \boldsymbol{\omega}) L_i(\mathbf{x}, \boldsymbol{\omega}) D(\mathbf{x}, \boldsymbol{\omega})\,\mathrm{d}\boldsymbol{\omega}\,\mathrm{d}\mu(\mathbf{x})\,, \tag{23}$$

where we have used $\mathcal{M} = \partial\mathcal{V} \cup \mathcal{V}$ to denote all points in the scene, and $\mathrm{d}\mu$ to represent volume (area) integration for medium (surface) points, respectively. We now proceed by recursively expanding the L_i term in the above equation and grouping the resulting terms. We express the resulting equations in standard three-point form; that is, we write $f(\mathbf{y} \to \mathbf{x})$ or $f(\mathbf{x} \leftarrow \mathbf{y})$ to mean $f(\mathbf{y}, \boldsymbol{\omega}_{\mathbf{yx}})$, and $f(\mathbf{x} \to \mathbf{y} \to \mathbf{z})$ to mean $f(\mathbf{y}, \boldsymbol{\omega}_{\mathbf{xy}}, \boldsymbol{\omega}_{\mathbf{yz}})$ where $\boldsymbol{\omega}_{\mathbf{xy}}$ denotes a unit-length vector from $\mathbf{x}$ to $\mathbf{y}$.

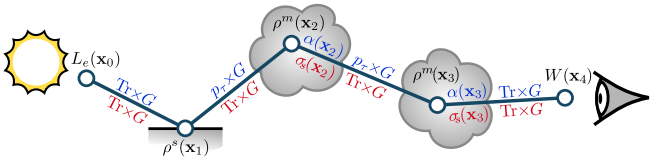

Fig. 3. A five vertex path with surface-to-surface ($\mathbf{x}_0\mathbf{x}_1$), surface-to-medium ($\mathbf{x}_1\mathbf{x}_2$), medium-to-medium ($\mathbf{x}_2\mathbf{x}_3$) and medium-to-surface ($\mathbf{x}_3\mathbf{x}_4$) transport. We show the terms of the path contribution function for the classical RTE (red) and our generalized RTE (blue). Shared terms are shown in black.

Expanding L_i yields an infinite sum of path integrals of the form

$$I = \sum_{k=1}^{\infty} \int_{\mathcal{P}_k} f(\overline{\mathbf{x}})\, \mathrm{d}\mu(\overline{\mathbf{x}}) = \int_{\mathcal{P}} f(\overline{\mathbf{x}})\, \mathrm{d}\mu(\overline{\mathbf{x}})\,, \tag{24}$$

where $\overline{\mathbf{x}} = \mathbf{x}_0 \dots \mathbf{x}_k$ represents a transport path with k segments and $k+1$ vertices (with the first vertex $\mathbf{x}_0$ on the light source, and the last vertex $\mathbf{x}_k$ on the sensor; see Figure 3), $\mathcal{P}_k$ is the space of all paths with k segments, and $\mathcal{P} = \bigcup_{i=1}^{\infty} \mathcal{P}_k$ is all of path space. The measure $\mathrm{d}\mu(\overline{\mathbf{x}})$ is a product measure corresponding to surface area and volume integration for surface and media vertices, respectively. The measurement contribution function $f(\overline{\mathbf{x}})$ is the product of emitted radiance (L_e), importance (W) and generalized path throughput (g):

$$f(\overline{\mathbf{x}}) = L_e(\mathbf{x}_0 \to \mathbf{x}_1) g(\overline{\mathbf{x}}) W(\mathbf{x}_{k-1} \leftarrow \mathbf{x}_k)\,, \tag{25}$$

with path throughput

$$g(\overline{\mathbf{x}}) = \Sigma(\mathbf{x}_0) \left[\prod_{i=1}^{k-1} \rho(\mathbf{x}_i)\right] \left[\prod_{i=0}^{k-1} T(\mathbf{x}_i, \mathbf{x}_{i+1}) G(\mathbf{x}_i, \mathbf{x}_{i+1})\right], \tag{26}$$

where $\rho(\mathbf{x}_i)$ is shorthand for $\rho(\mathbf{x}_{i-1} \to \mathbf{x}_i \to \mathbf{x}_{i+1})$, $G(\mathbf{x}', \mathbf{x}) = \frac{D(\mathbf{x}' \to \mathbf{x}) D(\mathbf{x} \to \mathbf{x}')}{\|\mathbf{x}' - \mathbf{x}\|^2} V(\mathbf{x}', \mathbf{x})$ is the generalized geometry term, and $V(\mathbf{x}', \mathbf{x})$ is the binary visibility function.

3.6 Comparison with Classical Light Transport

Given our generalized path integral above, it is useful to compare it to the path integral for the classical RTE. For classical exponential transport, a pixel measurement I is typically expressed using a path integral as in Equation (24) and (26), but with a different path throughput $g_c(\overline{\mathbf{x}})$:

$$g_c(\overline{\mathbf{x}}) = \left[\prod_{i=1}^{k-1} \rho_c(\mathbf{x}_i)\right] \left[\prod_{i=0}^{k-1} \mathrm{Tr}(\mathbf{x}_i, \mathbf{x}_{i+1}) G(\mathbf{x}_i, \mathbf{x}_{i+1})\right]. \tag{27}$$

In a classical medium, the exponential transmittance Tr replaces the transport kernel T, and the classical scattering function $\rho_c(\mathbf{x}_i)$ is:

$$\rho_c(\mathbf{x}_i) = \begin{cases} \rho^s(\mathbf{x}_{i-1} \to \mathbf{x}_i \to \mathbf{x}_{i+1})) & \text{if } \mathbf{x} \in \partial\mathcal{V} \\ \rho^m(\mathbf{x}_{i-1} \to \mathbf{x}_i \to \mathbf{x}_{i+1}) \sigma_s(\mathbf{x}_i) & \text{if } \mathbf{x} \in \mathcal{V} \end{cases}, \tag{28}$$

An apparent difference between these two throughputs is a factor of α in our equations where traditionally the scattering coefficient σ_s would appear. This is merely a notational preference, and the classical factor can be retrieved through a simple regrouping of terms. By expanding the transport kernel into the product $T(\mathbf{x}_i, \mathbf{x}_{i+1}) = E(\mathbf{x}_i, \mathbf{x}_{i+1}) \Sigma(\mathbf{x}_{i+1})$, we can match a $\Sigma(\mathbf{x}_i)$ to every scattering term $\rho(\mathbf{x}_i)$. If $\mathbf{x}_i$ lies in the medium, it holds that

$$\rho(\mathbf{x}_i) \Sigma(\mathbf{x}_i) = \rho^m(\mathbf{x}_i) \alpha(\mathbf{x}_i) \sigma_t(\mathbf{x}_i) = \rho_c(\mathbf{x}_i), \tag{29}$$

and a similar equivalence exists if $\mathbf{x}_i$ lies on a surface. Equation (26) can therefore be written:

$$g(\overline{\mathbf{x}}) = \Sigma(\mathbf{x}_0) \left[\prod_{i=1}^{k-1} \rho_c(\mathbf{x}_i)\right] \left[\prod_{i=0}^{k-1} E(\mathbf{x}_i, \mathbf{x}_{i+1}) G(\mathbf{x}_i, \mathbf{x}_{i+1})\right] \Sigma(\mathbf{x}_k)\,. \tag{30}$$

After regrouping, this path contribution looks very similar to the classical one. The Σ terms at emitter and sensor are due to a different emitter model in our theory, and can be removed by redefining L_e and W to be independent of the medium density. A major and important difference is an edge throughput E that replaces the classical transmittance term Tr. This term was obtained by reasoning about interaction probabilities and encapsulates the distinction between the free-flight PDF and the transmittance. It reduces to the classical transmittance term if we assume exponential free-flights, but allows energy conserving transport if we deviate from this assumption.

3.7 Energy Conservation

A proof of energy conservation for our theory follows from taking the transport equation (19) and showing that total energy before transport (L_o) is the same as total energy after transport (L_i).

We show the full mathematical details in the supplemental document, but the basic principle is to convert Equation (19) from gathering photons at scattering locations, to distributing photons from source locations. The derivation concludes in the following equality, which, if it holds, finishes the proof:

$$1 = \mathrm{Tr}(\tau(\mathbf{x}', \mathbf{x}_z)) + \int_0^{\tau(\mathbf{x}', \mathbf{x}_z)} p_\tau(\tau')\, \mathrm{d}\tau'\,. \tag{31}$$

This equation recalls Equation (6), which demonstrated that the classical RTE cannot be energy-conserving for a non-exponential transmittance. Compared to before, the result of our theory is a modified right-hand term, which represents the energy deposited in the medium. By differentiating between the free-flight PDF and the transmittance, the above equation is now always satisfied and guarantees energy conservation for any choice of p_τ.

3.8 Reciprocity

Earlier in this section, we alluded to the fact that our path integral is not reciprocal for non-exponential media. In the following paragraphs, we will first show a short proof of this fact, and then discuss the implications of this result.

Reciprocity refers to the property that the measurement does not depend on the direction of transport, i.e. the role of emitter and sensor can be swapped without changing the value of the measurement. Equivalently, we can say that the path throughput $g(\overline{\mathbf{x}})$ returns the same result if the path $\overline{\mathbf{x}}$ is reversed.

We now apply this principle to our path integral and compare the throughputs of a path and its reverse:

$$g(\mathbf{x}_0 \cdots \mathbf{x}_k) = g(\mathbf{x}_k \cdots \mathbf{x}_0)\,. \tag{32}$$

Cancelling reciprocal terms such as the geometry factor $G(\mathbf{x}_i, \mathbf{x}_{i+1})$ and scattering terms $\rho_c(\mathbf{x}_i)$ leaves

$$\prod_{i=0}^{k-1} E(\mathbf{x}_i, \mathbf{x}_{i+1}) = \prod_{i=0}^{k-1} E(\mathbf{x}_{i+1}, \mathbf{x}_i)\,. \tag{33}$$

For transport to be reciprocal, this equation should hold for any path. Consider now a two-vertex path $\mathbf{x}_0\mathbf{x}_1$ with $\mathbf{x}_0 \in \partial\mathcal{V}$ and $\mathbf{x}_1 \in \mathcal{V}$. Equation (33) simplifies to

$$E(\mathbf{x}_0, \mathbf{x}_1) = E(\mathbf{x}_1, \mathbf{x}_0) \tag{34}$$

$$p_\tau(\tau(\mathbf{x}_1, \mathbf{x}_0)) = \mathrm{Tr}(\mathbf{x}_0, \mathbf{x}_1). \tag{35}$$

The last equation states that our path integral is reciprocal as long as the transmittance is identical to the free-flight PDF. However, this can only be true if the transmittance is an exponential.

Discussion. At this point, it is worth discussing what reciprocity is and what it is not. Reciprocity is a convenient property that allows the same transport rules to be used for both importance and radiance; in practice, this allows for some simplification of bidirectional algorithms and can serve as a useful correctness test. However, lack of reciprocity does not mean non-physicality or exclusively unidirectional transport. There are many examples of generalizations of the RTE (e.g. multi-group simulations in neutron transport or fluorescence in light transport) that simulate physically valid systems, but are not self-adjoint.

Non-reciprocity still allows for bidirectional rendering algorithms, as long as quantities are evaluated in a consistent manner. In Section 6, we show how this can be achieved for our theory with relatively few changes to an existing rendering algorithm. We additionally show results rendered with unidirectional and bidirectional algorithms to demonstrate that consistent results can be achieved even though reciprocity does not hold.

In the end, reciprocity is a useful property, but it is not crucial for physically based transport. Other trade-offs are certainly possible, but for this particular generalization of the RTE, we have chosen to trade reciprocity in favor of non-exponential transmittance, which we see as a useful tool.

4 MODELING NON-EXPONENTIAL ATTENUATION

In Section 3 we established a theory of light transport which allowed arbitrary free-flight PDFs, and we showed how to easily modify standard path-sampling algorithms to leverage this new flexibility in Section 6. The last remaining question is how we should obtain, represent, and design such free-flight PDFs, and how we can physically interpret the corresponding light transport behavior.

It is common to model surface appearance at multiple scales, e.g. by representing large-scale variation using explicit geometry and displacements, while modeling fine-scale roughness statistically using a BRDF. Our theory allows a similar decomposition for volumes, where we model large-scale heterogeneous variation explicitly with spatially-varying macroscopic media properties $(\alpha(\mathbf{x}), \sigma_t(\mathbf{x}), \rho^m(\mathbf{x}))$, but we can additionally account for scatterer correlations or unresolved fine-scale heterogeneity *statistically* by modifying the free-flight PDF. Inspired by phenomenological [Ashikhmin and Shirley 2000; Phong 1975], data-driven [Ashikmin et al. 2000; Bagher et al. 2016; Matusik et al. 2003], and statistical microfacet [Blinn 1977; Cook and Torrance 1981] models for surface roughness, we can likewise obtain transmittance functions in different ways:

(1) The artist-driven "phenomenological" way (Section 4.1), where we directly design a free-flight PDF/transmittance free-hand or with simple parametric models;
(2) The "data-driven" physically based way (Section 4.2), where we instantiate a distribution of physical scatterers, and obtain the transmittance induced by these scatterers numerically (through sampling); and
(3) The "statistical" physically based way (Section 4.3) that seeks analytic parametric models for these functions driven by some statistical description of the distribution of the physical medium scatterers (Section 4.4).

4.1 Transmittance via directly designed free-flight PDFs

A simple phenomenological approach is to directly prescribe the free-flight PDF (7) to something other than an exponential. Table 1 lists the PDF $\mathrm{pdf}(x)$ and CDF $\mathrm{cdf}(x)$ of common statistical distributions. We can take any such distribution defined on the positive real line, and directly set $p_\tau(\tau) = \mathrm{pdf}(\tau)$. Equation (12) dictates that the transmittance should be the complement of the corresponding CDF, so we can set $\mathrm{Tr}(\tau) = 1 - \mathrm{cdf}(\tau)$.

We experimented with a variety of such distributions, including a step, linear ramp, sum of impulses, sum of exponentials, and Erlang-2. Figure 4 shows renderings and the corresponding parametric $\mathrm{Tr}(\tau)$ and $p_\tau(\tau)$ curves. It would also be possible to allow artists to design custom curves using a familiar graph editor interface.

The sum of two exponentials is particularly useful as the two exponents allow separately controlling the falloff of light near the start and tail of the distribution. Wrenninge et al. [2013] used this falloff for shadow rays to allow light to penetrate deeper, approximating multiple scattering. Our theory allows us to incorporate this in a consistent way for arbitrary bounces and light transport algorithms.

Inspired by this idea, we also took a classical monopole diffusion profile and interpreted it as a free-flight distribution. The radial falloff of a classical monopole is proportional to an Erlang-2 distribution with rate parameter $\lambda = \sqrt{3(1-\alpha)(1-g\alpha)}$ dependent on albedo α and the average cosine g. Simulating single scattering from a point light in a homogeneous medium with this transmittance profile would produce results similar to an all-bounce monopole diffusion approximation. Applied as a transmittance profile in our theory, this lets light penetrate further into the medium at each bounce, and allows us to approximate multiple-scattered transport using fewer explicitly simulated bounces.

4.2 Data-driven transmittance via ensemble averaging

While directly designing transmittance functions in this top-down approach provides high-level artistic controls, it may not correspond to any physically realizable distribution of scattering particles. To obtain physically justifiable profiles, we can instead prescribe the unresolved statistical properties of the medium, and deduce the profiles this gives bottom-up. We will denote these unresolved statistical properties with a subscript μ and, to simplify the exposition, we will for now assume that the macroscopic medium properties

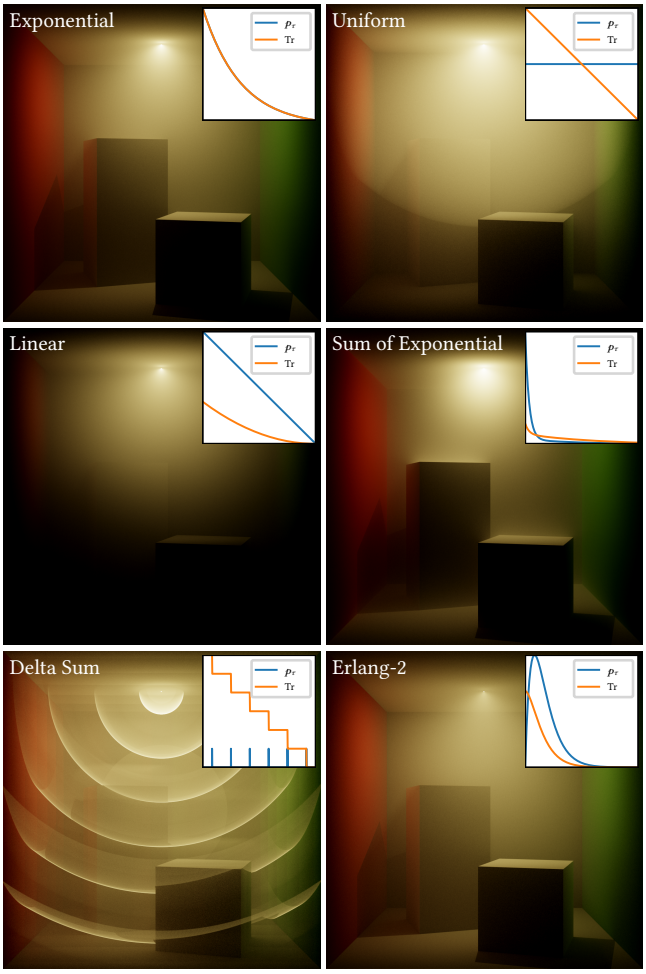

Fig. 4. We show a homogeneous medium in a Cornell Box rendered with six different free-flight PDFs. These are: Exponential p_τ^{exp} (top left), uniform $\mathcal{U}(0, 3/4)$ (top right), linear $\mathcal{L}(0, 3/4)$ (middle left), sum of two exponentials (middle right), delta sum $\text{Ш}(6)$ (bottom left), and Erlang-2 $\mathcal{E}(2)$ (bottom right). Compared to the exponential baseline (top left), we can achieve a wide range of appearances through simple parametric transmittance curves.

are homogeneous with $\sigma_t = 1$ so that macroscopic optical depths τ and distances are equivalent. We will derive free-flight PDFs $p_\mu(t)$ or transmittance functions $\text{Tr}_\mu(t)$ arising from these statistical properties initially in terms of distance t. In Section 6, we will combine these two scales and parameterize the functions using the macroscopic optical depth τ instead of distance t, giving us the free-flight PDFs $p_s(\tau)$ and transmittances $\text{Tr}(\tau)$ we desire.

4.2.1 Ensemble-averaging discrete media/particles. One physically based approach would be to explicitly construct a discrete collection of scattering *particles* (Figure 2) and compute the transmittance as:

$$\left\langle \text{Tr}_\mu(t) \right\rangle = \left\langle V_\mu(\mathbf{x}, \mathbf{x} + t\boldsymbol{\omega}) \right\rangle \approx \frac{1}{N} \sum_{i=1}^{N} V_{\mu_i}(\mathbf{x}_i, \mathbf{x}_i + t\boldsymbol{\omega}_i), \tag{36}$$

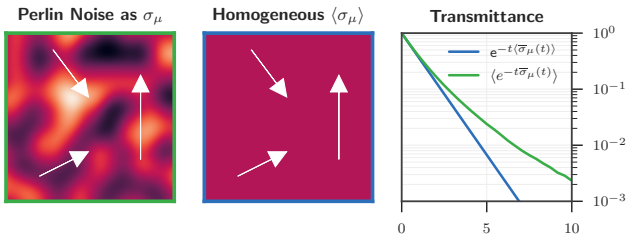

Fig. 5. Micro-scale density σ_μ modeled as 3D perlin noise. We visualize a 2D slice (left), a homogeneous medium with equivalent mean density (middle), and the ensemble-averaged transmittance along random rays—visualized as white arrows—and instantiations of the media (right). It has a longer tail than the transmittance through the averaged medium due to Jensen's inequality.

where V_μ denotes the visibility within a distribution of micro-scale particles, and $\langle \cdot \rangle$ denotes an *ensemble average*, which can be approximated using the Monte Carlo estimator on the right by generating random rays $\mathbf{x}_i, \boldsymbol{\omega}_i$ through different realizations of the micro-scale particle distributions μ_i.

The ensemble average in Equation (36) is computing the probability of having no scattering particles over a distance t along a random ray. If the positions of the particles are statistically independent, then this tabulation procedure will converge to the exponential distribution (see Figure 2a,e), since it is computing the probability of no events occurring over a distance t within a Poisson process. However, it is also possible to instantiate points with specially crafted spatial correlations that e.g. induce or inhibit clumping. Figure 2e visualizes the transmittance curves obtained from 2D discrete points sets with spectral power falloffs corresponding to "blue" (b), "pink" (c) and "red" (d) noise respectively. Data-driven curves like these are a "gold standard" in the sense that they can handle any distribution of scatterers we can explicitly construct. But they require expensive sampling and tabulation for every set of parameters, which quickly becomes intractable for large collections of particles in higher dimensions.

4.2.2 Ensemble-averaging continuous densities. We can forego instantiating discrete particles and instead model the spatial correlations via a heterogeneous micro-scale density field $\sigma_\mu(\mathbf{x})$ (see Figure 5). Given a fixed realization of $\sigma_\mu(\mathbf{x})$, the micro-scale transmittance to a distance t along a fixed ray $\mathbf{x}, \boldsymbol{\omega}$ is:

$$\text{Tr}_\mu(\mathbf{x}, \boldsymbol{\omega}; t) = \mathrm{e}^{-\tau_\mu(\mathbf{x}, \boldsymbol{\omega}; t)}, \tag{37}$$

$$\text{where} \quad \tau_\mu(\mathbf{x}, \boldsymbol{\omega}; t) = \int_0^t \sigma_\mu(\mathbf{x} + \boldsymbol{\omega} t')\, \mathrm{d}t' \tag{38}$$

is the micro-scale optical depth. We can equivalently write:

$$\text{Tr}_\mu(\mathbf{x}, \boldsymbol{\omega}; t) = \mathrm{e}^{-s\overline{\sigma}_\mu(\mathbf{x}, \boldsymbol{\omega}; t)}, \tag{39}$$

$$\text{where} \quad \overline{\sigma}_\mu(\mathbf{x}, \boldsymbol{\omega}; t) = \frac{\tau_\mu(\mathbf{x}, \boldsymbol{\omega}; t)}{t} = \frac{1}{t} \int_0^t \sigma_\mu(\mathbf{x} + \boldsymbol{\omega} t')\, \mathrm{d}t' \tag{40}$$

is the micro-scale density field $\sigma_\mu(\mathbf{x})$ averaged along a line segment of length t between $\mathbf{x}$ and $\mathbf{x} + t\boldsymbol{\omega}$.

Table 1. The probability density functions $\mathrm{pdf}(x)$, cumulative distribution function $\mathrm{cdf}(x)$, and characteristic functions $\varphi(r)$ for a variety of statistical distributions. $\Gamma(\alpha)$ and $\gamma(s, x)$ are the complete and lower incomplete gamma functions, and $\delta(x)$ and $H(x)$ are the Dirac delta and Heaviside step functions. When μ is used as a parameter it specifies the mean of the corresponding PDF. We omit the implicit values of 0 or 1 in PDFs and CDFs with bounded support. When hand-designing attenuation via free-flight distributions, $\mathrm{pdf}(\tau)$ describes the free-flight distribution, and transmittance is obtained via $\mathrm{Tr}(\tau) = 1 - \mathrm{cdf}(\tau)$. When designing attenuation via $1/f$ noise, $\mathrm{pdf}(\overline{\sigma}_\mu)$ describes the distribution of $\overline{\sigma}_\mu$ due to fBm micro-fluctuations, transmittance is obtained from $\varphi(\mathrm{i}\tau)$, and the free-flight distribution becomes $-\mathrm{d}\varphi(\mathrm{i}\tau)/\mathrm{d}\tau$. The last two columns list sampling routines for these two approaches.

					Sampling	
Distribution	Parameters	$\mathrm{pdf}(x)$	$\mathrm{cdf}(x)$	$\varphi(r)$	$x_i \propto \mathrm{pdf}(x)$	$\propto -\mathrm{d}\varphi(\mathrm{i}r)/\mathrm{d}r$
Delta δ_μ	mean: $\mu > 0$	$\delta(x-\mu)$	$H(x-\mu)$	$\mathrm{e}^{\mathrm{i}r\mu}$	$x_\delta = \mu$	$-\frac{\ln \xi}{x_\delta}$
DeltaSum III(n)	impulses: $\{\mu_1, \dots \mu_n\}$	$\frac{1}{n}\sum_{i=1}^n \delta(x-\mu_i)$	$\frac{1}{n}\sum_{i=1}^n H(x-\mu_i)$	$\frac{1}{n}\sum_{i=1}^n \mathrm{e}^{\mathrm{i}r\mu_i}$	$x_{\mathrm{III}} = $ uniform from $\{\mu_1, \dots \mu_n\}$	$-\frac{\ln \xi}{x_{\mathrm{III}}}$
Uniform $\mathcal{U}(a,b)$	range: $0 < a < x < b < \infty$	$\frac{1}{b-a}$	$\frac{x-a}{b-a}$	$\frac{\mathrm{e}^{\mathrm{i}rb} - \mathrm{e}^{\mathrm{i}ra}}{\mathrm{i}r(b-a)}$	$x_u = (b-a)\xi + a$	$-\frac{\ln \xi_2}{x_u}$
Linear $\mathcal{L}(b)$	range: $0 < x < b < \infty$	$\frac{2}{b}\left(1 - \frac{x}{b}\right)$	$1 - 2\frac{x}{b} - \frac{x^2}{b^2}$	—	$x_l = b(1-\sqrt{\xi})$	$-\frac{\ln \xi_2}{x_l}$
Normal $\mathcal{N}(\mu, v)$	mean: $0 \le \mu < \infty$ variance: $v > 0$	$(2\pi v)^{-\frac{1}{2}} \mathrm{e}^{-\frac{(x-\mu)^2}{2v}}$	$\frac{1}{2}\left[1 + \mathrm{erf}\left(\frac{x-\mu}{\sqrt{2v}}\right)\right]$	$\mathrm{e}^{\mathrm{i}r\mu - r^2 v/2}$	$x_n = \sqrt{-2\ln\xi_1}\,\cos(2\pi\xi_2)$	$-\frac{\ln \xi_2}{x_n}$
Gamma $\Gamma(\mu, \alpha)$	mean: $0 \le \mu < \infty$ shape: $\alpha > 0$	$\frac{1}{\Gamma(\alpha)}\left(\frac{\alpha}{\mu}\right)^\alpha x^{\alpha-1}\mathrm{e}^{-x\alpha/\mu}$	$\frac{1}{\Gamma(\alpha)}\gamma(\alpha, x\alpha/\mu)$	$(1 - \mathrm{i}r\mu/\alpha)^{-\alpha}$	Marsaglia's method	$(\xi^{-1/\alpha} - 1)\,\alpha/\mu$
Erlang-2 $\mathcal{E}(\lambda)$	rate: $\lambda > 0$ shape: $k \in \mathbb{N}$	$\lambda^2 x \mathrm{e}^{-\lambda x}$	$\mathrm{e}^{-\lambda x} + \lambda x \mathrm{e}^{-\lambda x}$	$(1 - \mathrm{i}r/\lambda)^{-2}$	$x_{\mathcal{E}} = -\frac{1}{\lambda}\ln(\xi_1\xi_2)$	$(\xi^{-1/2} - 1)\,\lambda$

As in the discrete case, we can consider the ensemble-average of transmittance (37) for a fixed distance t:

$$\left\langle \mathrm{Tr}_\mu(t) \right\rangle = \left\langle \mathrm{e}^{-t\overline{\sigma}_\mu(\mathbf{x},\boldsymbol{\omega};t)} \right\rangle \approx \frac{1}{N}\sum_{i=1}^N \mathrm{e}^{-t\overline{\sigma}_{\mu_i}(\mathbf{x}_i,\boldsymbol{\omega}_i;t)}, \tag{41}$$

or similarly in terms of τ_μ using Equation (37). The Monte Carlo estimate is averaging values returned by $\overline{\sigma}_\mu(\mathbf{x}, \boldsymbol{\omega}; t)$ for a *fixed* t, but over random rays $(\mathbf{x}_i, \boldsymbol{\omega}_i)$ and realizations of the medium μ_i. Figure 5 shows the ensemble-averaged transmittance $\left\langle \mathrm{Tr}_\mu(t) \right\rangle$ of a Perlin noise-controlled micro-scale density σ_μ and Figure 7 illustrates random 1D transects and line averages $\overline{\sigma}_\mu$ thereof.

While computing ensemble-averaged transmittance this way avoids the complexities of instantiating billions of discrete particles, it still makes parametric control cumbersome due to the need for tabulation.

4.3 Probabilistic ensemble-averaging

We can instead take a probabilistic view by treating $\overline{\sigma}_\mu(t)$ (or $\tau_\mu(t)$) as a random variable, where we drop the explicit dependence on $\mathbf{x}$ and $\boldsymbol{\omega}$ due to the ensemble averaging.

Longer-than-exponential tails. This allows us to explain why in Figure 5 the ensemble-averaged transmittance (bottom, green) results in a longer tail than the exponential (bottom, blue). Jensen's inequality states that for a random variable X and a concave function f: $\langle f(X) \rangle \ge f(\langle X \rangle)$. Substituting the exponential for f, and $\overline{\sigma}_\mu(t)$ for X, we should therefore expect:

$$\left\langle \mathrm{e}^{-t\overline{\sigma}_\mu(t)} \right\rangle \ge \mathrm{e}^{-t\left\langle \overline{\sigma}_\mu(t) \right\rangle}. \tag{42}$$

This will be an equality iff $\overline{\sigma}_\mu(t) = \left\langle \overline{\sigma}_\mu(t) \right\rangle$ for all t, which would mean the medium had no density fluctuations (was homogeneous) to begin with.

Link to characteristic functions. Since $\overline{\sigma}_\mu$ is a random variable, it has some probability density, which we denote $\mathrm{pdf}(\overline{\sigma}_\mu \mid t)$. This PDF describes the variability of $\overline{\sigma}_\mu$ as a function of distance t, which we visualized as histograms on the right-hand side of Figure 7.

We can now write the ensemble average as the integral:

$$\left\langle \mathrm{Tr}_\mu(t) \right\rangle = \left\langle \mathrm{e}^{-t\overline{\sigma}_\mu(t)} \right\rangle = \int_0^\infty \mathrm{e}^{-t\overline{\sigma}_\mu}\, \mathrm{pdf}(\overline{\sigma}_\mu \mid t)\, \mathrm{d}\overline{\sigma}_\mu. \tag{43}$$

This takes a form remarkably similar to the *characteristic function* (CF), which is the Fourier transform of a random variable's PDF:

$$\varphi_X(r) = \left\langle \mathrm{e}^{\mathrm{i}rX} \right\rangle = \int_{\mathbb{R}} \mathrm{e}^{\mathrm{i}rx}\, \mathrm{pdf}_X(x)\, \mathrm{d}x, \tag{44}$$

where $\mathrm{i} = \sqrt{-1}$ is the imaginary constant. Comparing Equation (44) to (43), we see that for a fixed t the ensemble-averaged transmittance is simply the CF of the random variable $\overline{\sigma}_\mu$ (by passing in $t\mathrm{i}$ for r):[1]

$$\left\langle \mathrm{Tr}_\mu(t) \right\rangle = \varphi_{\overline{\sigma}_\mu(t)}(t\mathrm{i}). \tag{45}$$

This is a very powerful tool, because, as long as we can express the variation of $\overline{\sigma}_\mu$ (or τ_μ) using a distribution with a well-known CF (see Table 1), we can obtain closed-form expressions for the ensemble-averaged transmittance! Note that the parameters of the distribution $\mathrm{pdf}(\overline{\sigma}_\mu \mid t)$ may depend on the distance t, as we saw in Figure 7.

Discussion. So what should this distribution, and its dependence on t be? We could simply choose a convenient PDF and allow an artist to set its (potentially t-dependent) parameters by hand. While this would be fully parametric and analytic, it is unclear how (or whether) such a model would correspond to any micro-scale density fluctuations or correlations. Alternatively, we could ensure correspondence by fitting the distribution and its t-dependent parameters to tabulated data from realizations of $\overline{\sigma}_\mu(t)$, like in Figure 7. Next, we will instead leverage recent work by Davis and colleagues [2011; 2014] to obtain a parametric, closed-form transmittance function

[1] We could also express this using *moment generating functions* (MGFs), which are defined similarly to the CF, but without the imaginary constant.

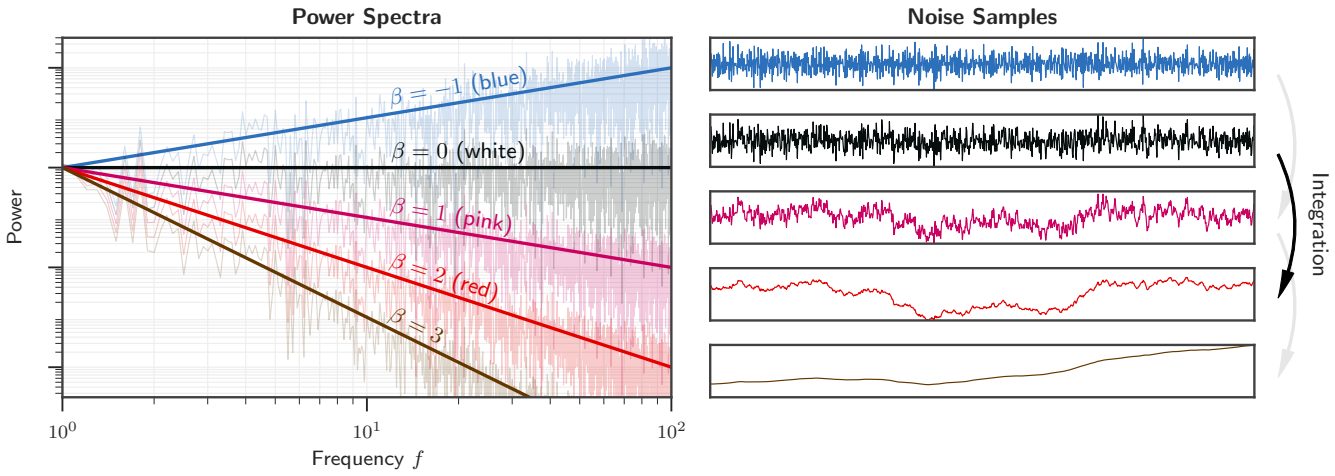

Fig. 6. $1/f^\beta$ noise (right) is characterized by a spectral exponent β which determines the slope of its power spectrum on a log-log plot (left). Qualitatively, different values of β lead to noises of different "roughnesses" (right), and integrating a noise with spectral exponent β (e.g. white noise) produces another noise with spectral exponent $\beta + 2$ (e.g. red noise).

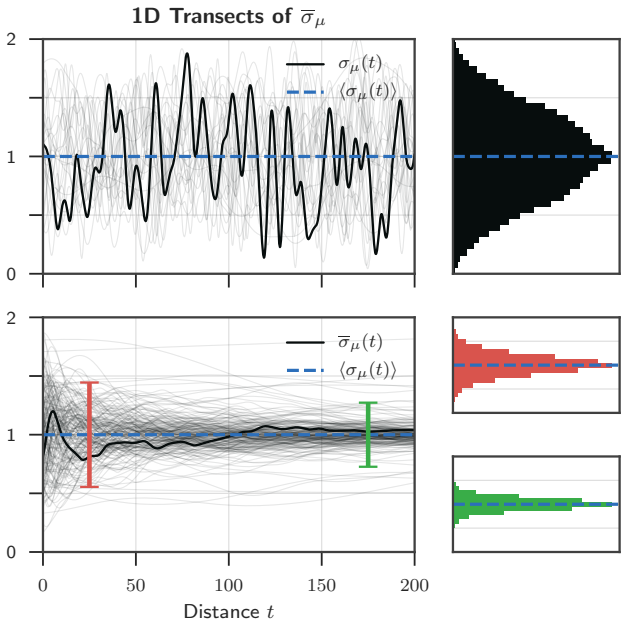

Fig. 7. 1D transects of a Perlin noise micro-scale density function $\sigma_\mu(t)$ for random rays and realizations, a single sample of which is highlighted in black (top). σ_μ is a random variable, the distribution of which, $\text{pdf}(\sigma_\mu)$ is illustrated by the histogram on the right. The line-averaged micro-scale density $\overline{\sigma}_\mu(t)$ (bottom) is likewise a random variable, but the distribution now potentially depends on the length of the line segment t. We show histograms of the distribution of $\text{pdf}(\overline{\sigma}_\mu(t))$ at $t = 2.5$ (red) and $t = 22.5$ (green).

whose parameters provide a physical interpretation of the underlying micro-scale extinction field as a fractal medium.

4.4 Closed-form average transmittance in fractal media

We will follow Davis and Mineev-Weinstein [2011] and model the variability in $\sigma_\mu(\mathbf{x})$ as a 3D fractal with 1D transects $\sigma_\mu(x)$ characterized by $1/f^\beta$ fractal noise. Figure 6 provides a visual explanation: Qualitatively, β determines how "rough" the noise will be (right), while quantitatively it dictates that the falloff of the function's power spectrum will be $1/f^\beta$ (left). This directly controls the spatial correlations, where $\beta = 0$ means uncorrelated "white" noise, while $\beta > 0$ and $\beta < 0$ produce positive and negative correlations respectively.

We model $\sigma_\mu(x)$ statistically as a noise defined by: a mean μ_σ, a constant C controlling its overall amplitude, and its spectral exponent $-1 \le \beta \le 1$ ranging from "blue" ($\beta = -1$) to "pink" ($\beta = 1$). For convenience, we will combine these into a parameter vector $\psi = \{\mu_\sigma, C, \beta\}$. This allows us to write the ensemble-averaged transmittance (43) as:

$$\left\langle \text{Tr}_\mu(t \mid \psi) \right\rangle = \int_0^\infty \mathrm{e}^{-t\overline{\sigma}_\mu} \, \text{pdf}(\overline{\sigma}_\mu \mid t, \psi) \, \mathrm{d}\overline{\sigma}_\mu, \tag{46}$$

where the PDF is now determined by the distance t and parameters $\psi = \{\mu_\sigma, C, \beta\}$ defining the medium.

Given this fractal noise model, what can we say about $\text{pdf}(\overline{\sigma}_\mu \mid t, \psi)$?

Gaussian $1/f^\beta$ noise. A key property of Gaussian $1/f^\beta$ noise is that it produces fractional Brownian motion (fBm) [Mandelbrot and Ness 1968] with $\beta + 2$ via integration (arrows in Figure 6).[2] We therefore know that $\tau_\mu(t)$ will be a noise with $1 \le \beta_\tau \le 3$ and its distribution (as well as that of $\overline{\sigma}_\mu$) will be a Gaussian. Davis and Mineev-Weinstein [2011] formally derived the dependence of this Gaussian on the distance t and medium parameters ψ:

$$\text{pdf}(\overline{\sigma}_\mu \mid t, \psi) = \mathcal{N}(\mu_\sigma, v_{\overline{\sigma}_\mu}(t)), \quad \text{with} \quad v_{\overline{\sigma}_\mu}(t) = (C\mu_\sigma)^{\beta+1} t^{\beta-1}. \tag{47}$$

[2] β is directly related to the Hurst parameter $H = (\beta - 1)/2$ more commonly use in the fractal literature [Barnsley et al. 1988] when describing fBm and the "persistence" parameter of fractal Perlin noise [Ebert et al. 2002] used in graphics.

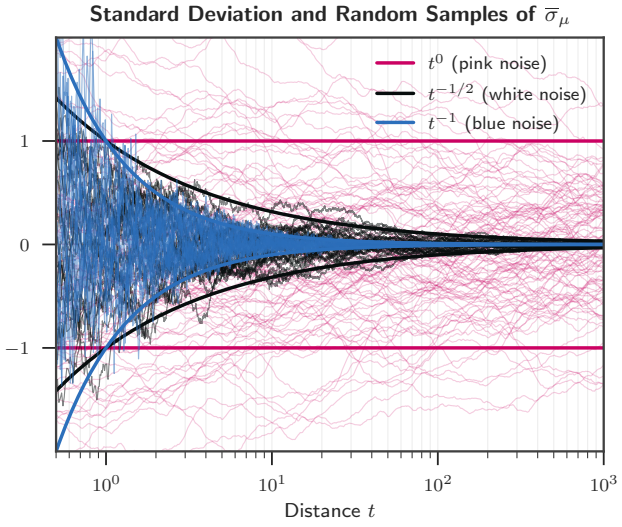

Fig. 8. Random samples of the line-averaged micro-scale density $\overline{\sigma}_\mu(t)$ (thin transparent lines) and the standard deviation thereof (thick opaque lines). When the micro-scale density $\sigma_\mu(t)$ is modeled as Gaussian $1/f^\beta$ noise, the spectral exponent β directly controls the variance $v_{\overline{\sigma}_\mu}(t)$ as a function of distance t, where lower values of β lead to more rapid decay. "Pink" noise (where $\beta = 1$), is scale-invariant meaning that $v_{\overline{\sigma}_\mu}$ is independent of t.

Figure 8 visualizes random transects of $\overline{\sigma}_\mu(t)$: the medium σ_μ averaged over a distance t. This figure shows the same information as the second row of Figure 7, but this time for media modeled as fractal noise with $\beta = -1, 0, 1$. The superimposed analytic curves plot the standard deviation $\sqrt{v_{\overline{\sigma}_\mu}}(t)$ from Equation (47) as a function of t, matching the behavior of the random transects well.

Using the characteristic function of the normal distribution (Table 1) with these parameters, we can obtain a close-formed expression for the ensemble-averaged transmittance via Equation (45):

$$\left\langle \mathrm{Tr}_\mu(t \mid \psi) \right\rangle \approx \mathrm{e}^{-\mu_\sigma t + v_{\overline{\sigma}_\mu}(t) t^2/2} = \mathrm{e}^{-\mu_\sigma t + (C\mu_\sigma t)^{\beta+1}/2} \tag{48}$$

Unfortunately, this is only an approximation because the Gaussian is supported on the entire real line, but values of $\sigma_\mu < 0$ are non-physical. This model for noise is therefore only reasonable when μ_σ is set sufficiently high and v set sufficiently low so that negative extinction coefficients are unlikely to occur.

Gamma-distributed $1/f^\beta$ noise. To counteract the artifacts arising due to these negative intrusions, Davis and Mineev-Weinstein [2011] proposed modeling the distribution of extinction values σ_μ with the strictly non-negative Gamma distribution $\mathrm{pdf}(\overline{\sigma}_\mu \mid t, \psi) = \Gamma(\mu_\sigma, \alpha(t))$, with parameters set to match the mean and variance of the Gaussian model. Combining Equation (45) with Table 1 gives:

$$\left\langle \mathrm{Tr}_\mu(t \mid \psi) \right\rangle = \varphi_{\Gamma_{t,\psi}}(t\mathrm{i}) = \left(1 + \frac{\mu_\sigma t}{\alpha(t)}\right)^{-\alpha(t)}, \tag{49}$$

$$\text{where} \qquad \alpha(t) = \frac{\mu_\sigma^2}{v_{\overline{\sigma}_\mu}(t)} = \frac{(\mu_\sigma t)^{1-\beta}}{C^{1+\beta}} \tag{50}$$

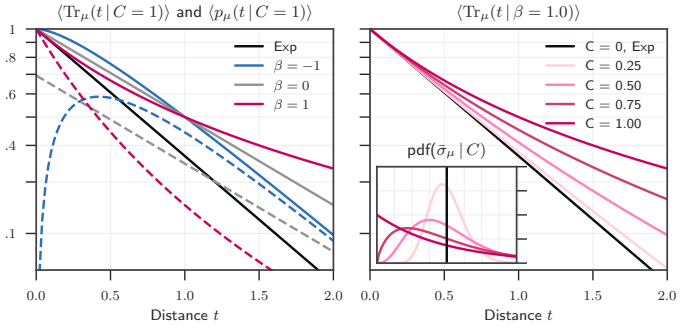

Fig. 9. Ensemble-averaged transmittance curves ($\mathrm{Tr}_\mu(t)$ solid) and free-flight PDFs ($p_\mu(t)$, dashed) in $1/f^\beta$ noise, left: for a fixed $C = 1$ and different values of β; and right: for $\beta = 1$ and different values of C. The inset on the right shows how different values of C influence $\mathrm{pdf}(\overline{\sigma}_\mu)$ for pink noise.

is the Gamma model's shape parameter that enforces a variance dictated by Equation (47).

Discussion. Equation (49) provides a simple 3-parameter model to produce non-exponential transmittance functions by specifying the mean extinction μ_σ, the overall amplitude of variation C, and the color/spectral falloff/correlation of the noise β. Figure 9 visualizes Equation (49) for various β and C, but a fixed $\mu_\sigma = 1$.

As we would hope, both the Gaussian (48) and Gamma (49) models reduce to a simple exponential when variance $v \to 0$ (and hence $\alpha \to \infty$). This will happen if the medium is actually homogeneous ($C = 0$), or if we have white noise ($\beta = 0$), both of which correspond to independent scatterers. In the latter case of white noise, we obtain exponential falloff, but with a modified extinction coefficient.

"Pink" $1/f$ noise (when $\beta = 1$) is another interesting case because it has a "scale-invariant" property where the distribution $\mathrm{pdf}(\overline{\sigma}_\mu)$ no longer depends on t (see Figure 8). The variance that plugs into Equation (48) and (49) reduces to $v_{\overline{\sigma}_\mu} = C^2\mu_\sigma^2$, and so α also no longer depends on t. In this case, ensemble averaging transmittance over a heterogeneous medium can be equivalently interpreted as averaging transmittance across a continuum of *homogeneous* media, each with a random, but spatially homogeneous extinct coefficient drawn from the distribution $\mathrm{pdf}(\overline{\sigma}_\mu)$.

5 COMBINING MACRO- AND MICRO- PROPERTIES

Section 4 presented a variety of ways to obtain new transmittance functions. Some of these functions, such as user-designed curves, can be used directly. However, ensemble-averaged transmittances $\left\langle \mathrm{Tr}_\mu(t) \right\rangle$ are defined in terms of distance t rather than optical depth τ, and it is not immediately clear how to combine the micro-scale and macro-scale heterogeneity. In this section, we therefore first show how to convert these transmittance functions so that they can be used in our framework, and offer a physical interpretation of this conversion. We then show how these transmittance functions can be implemented in a traditional Monte Carlo rendering algorithm.

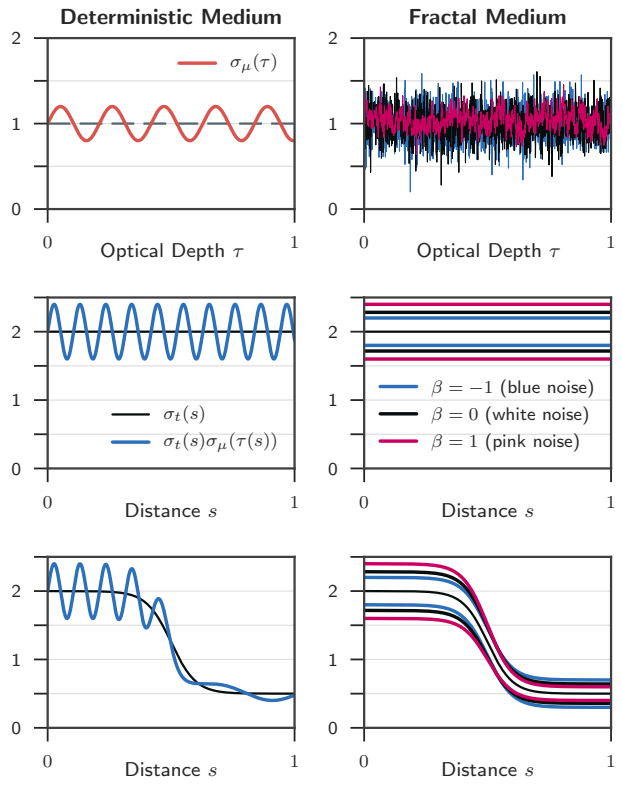

Fig. 10. We express volumetric micro-roughness $\sigma_\mu(\tau)$ (top) statistically and model macro-scale extinction $\sigma_t(s)$ explicitly (black, homogeneous: middle, heterogeneous: bottom) and combine them (blue). Since we define micro properties with respect to macroscopic optical depth, the statistical fluctuations/correlations $\sigma_\mu(\tau)$ represents are scaled vertically and squeezed horizontally by the local extinction coefficient (left column). The statistical behavior of rescaled fractal noise depends on its power spectrum via Equation (53). For instance, the standard deviation of blue noise ($\beta = -1$) does not depend on σ_t, while for pink noise ($\beta = 1$) it is proportional to σ_t. The right column illustrates this relationship for $\beta = -1, 0, 1$.

One way of viewing the ensemble-averaging process is that we replace a (discrete or continuous) heterogeneous medium with exponential transmittance Tr by a homogenized medium with non-exponential transmittance $\langle \mathrm{Tr}_\mu(t) \rangle$. The extinction coefficient of this homogenized medium is μ_σ, i.e. the average extinction of the original heterogeneous medium. In this homogenized world, distance and optical depth are connected with the simple relation $\tau = t \cdot \mu_\sigma$. Then we can easily define the ensemble-averaged transmittance with respect to τ:

$$\mathrm{Tr}(\tau) = \left\langle \mathrm{Tr}_\mu\left(\tau/\mu_\sigma\right) \right\rangle. \tag{51}$$

Now that this transmittance is defined in terms of optical depth, we can insert the macro-scale optical depth $\tau(\mathbf{x}, \mathbf{x}')$ in the above equation to combine the macro-scale and (statistical) micro-scale heterogeneity.

5.1 Physical interpretation.

How can we interpret this combined medium?

Deterministic micro-scale media. Let us first assume that the macro-scale medium is homogeneous with density $\sigma_t = 2$ (Figure 10 middle-left) and the ensemble averaged transmittance was obtained from a single realization of a fluctuating function with a mean $\mu_\sigma = 1$ (Figure 10 top-left). By mapping the transmittance through the macro-scale optical depth, the micro-scale function is scaled vertically so that its mean μ_σ matches that of the macro-scale density σ_t, and simultaneously it is squished horizontally since small steps in macroscopic optical depth map to larger distances in the micro-scale medium. For heterogeneous macro-scale media the amount of this stretching is determined by the local ratio of the macro-scale extinction to the micro-scale mean: $\sigma_t(t)/\mu_\sigma$ (Figure 10 bottom-left).

Stochastic fractal micro-scale media. With ensemble averaged transmittance from fractal media, we can only reason about the micro-density function in a statistical sense, and this physical interpretation changes slightly. Firstly, due to the self-similar nature of $1/f^\beta$ fractal noise, horizontal squeezing and stretching has no effect on the wavelength content and can be ignored. Instead, we can see from Equations (48,49) that scaling the distance t by some constant c is equivalent to scaling the mean μ_σ by the same constant:

$$\left\langle \mathrm{Tr}_\mu\left(c\, t \mid \{\mu_\sigma, C, \beta\}\right) \right\rangle = \left\langle \mathrm{Tr}_\mu\left(t \mid \{c\, \mu_\sigma, C, \beta\}\right) \right\rangle. \tag{52}$$

This means that – as in the deterministic case – Equation (51) adjusts the mean μ_σ of the micro-scale medium to locally match the density σ_t at the macro-scale. Changing just the mean μ_σ of the noise, however, changes its standard deviation in a β-dependent way:

$$\sqrt{\frac{v_{\overline{\sigma_\mu}}\left(t \mid \{c\, \mu_\sigma, C, \beta\}\right)}{v_{\overline{\sigma_\mu}}\left(t \mid \{\mu_\sigma, C, \beta\}\right)}} = \sqrt{c^{\beta+1}}. \tag{53}$$

This suggests that the way the density match is achieved has a different interpretation based on the color of the noise (Figure 10 right). For both the deterministic case and "pink" noise ($\beta = 1$), Equation (51) corresponds to *scaling* the micro-fluctuations vertically by c, but as β decreases the standard deviation is scaled less, until at "blue" noise ($\beta = -1$) it is not scaled at all ($c^0 = 1$), suggesting a vertical *shift/translation* of the noise instead.

6 IMPLEMENTATION

In this section, we give a brief outline of the modifications that need to be made to an existing rendering algorithm to support our theory. For now, we assume that we are given an opaque distance-sampling procedure `sample_distance(`ξ`)`, which returns a distance s given random number ξ, as well as functions `distance_pdf(`s`)` and `distance_cdf(`s`)` that express the PDF and CDF of the sampled distance. We later expand on possible choices for this sampling procedure.

Note that the free-flight PDF and the distance sampling PDF are unrelated; the former is a physical property of the medium, whereas the latter is an implementation detail of the rendering algorithm. In practice, they can be chosen to be identical as a noise reduction measure, but this is not required by the theory.

We outline the procedure for edge evaluation and sampling in Algorithm 1. Evaluating $E(\mathbf{x}_i, \mathbf{x}_{i+1})$ requires vertices to be specified in consistent order from the light source, but practical rendering algorithms usually order vertices in the direction in which the path is traced. To ensure consistent evaluation, we require an additional *adjoint* flag specifying the direction of transport. If the edge endpoint (from the perspective of the light source) lies on a surface, the transmittance is returned, and the free-flight PDF otherwise.

Sampling edge vertices proceeds by sampling a random distance s and deciding whether it lies beyond the nearest surface. If it is (with probability $1 - \texttt{distance\_cdf}(s)$), the surface vertex $\mathbf{x}_z$ is generated; otherwise (with probability density $\texttt{distance\_pdf}(s)$), a medium vertex $\mathbf{x}_s$ is generated. The sampling weight is obtained by dividing the edge throughput by the sample probability.

Algorithm 1: Edge throughput evaluation and sampling in our theory

```
function E(x, x′, adjoint)
    endpoint ← adjoint ? x : x′
    if endpoint ∈ ∂V then
        return Tr(x, x′)
    else
        return p_τ(τ(x, x′))
function sample(x_i, ω, ξ, adjoint)
    z ← raytrace(x_i, ω)
    s ← sample_distance(ξ)
    if s < z then
        pdf = distance_pdf(s)
    else
        pdf = 1 − distance_cdf(s)
    weight = E(x_i, x_{i+1}, adjoint)/pdf
    x_{i+1} ← x_i + min(s, z) · ω
    return {weight, x_{i+1}}
```

6.1 Distance Sampling

Algorithm 1 works for any distance sampling PDF. For efficiency reasons, this PDF should be chosen to be as proportional to E as possible.

In our implementation, we use a simple procedure to obtain distances distributed proportionally to p_s. We first sample an optical depth τ^* with density proportional to $p_\tau(\tau^*)$. We do this analytically using Table 1 for all directly designed free-flight PDFs and for those based on $1/f$ noise when $\beta = 1$. For $\beta \neq 1$, we numerically invert the CDF $= 1 - \mathrm{Tr}(\tau)$ with binary search.

We then solve for the distance s such that $\tau^* = \tau(\mathbf{x}, \mathbf{x}_s)$, either exactly (trivial in homogeneous media, and using regular tracking in heterogeneous media) or approximately (using raymarching).

When tracing radiance, the resulting edge weight is $1/\sigma_t(\mathbf{x}_s)$ if the sampled vertex lies in the medium, and is 1 if the vertex lies on a surface. This is an optimal sampling strategy, but *only* for paths traced from the light source. For paths traced from the camera, the edge throughput is evaluated in reverse order compared to the distance sampling PDF, and does not necessarily cancel. Since regular tracking and raymarching are expensive on high-resolution data, we probabilistically terminate transmittance evaluation at each step with Russian Roulette if its value is close to zero.

For some of our scenes (Figure 4), the additional noise from distance sampling is negligible; for others (Figures 1, 12, 13), we optionally sample the optical depth τ^* proportionally to $\mathrm{Tr}(\tau^*)$ for the first segment traced from the camera.

As sampling is not the focus of our paper, we did not further investigate this topic. However, the sampling strategies we use leave ample space for improvement, and we hope to address this in future work.

7 RESULTS

We implemented our theory in two existing rendering systems, PBRTv3 [Pharr et al. 2016] and Tungsten [Bitterli 2018], following the outline in Section 6.

In Figure 4, we show a homogeneous medium rendered with five different designed transmittance curves and compare the results to an exponential medium. The non-exponential transmittances are simple parametric functions, such as linear or quadratic curves, but lead to a wide range of appearances that cannot be reproduced by the exponential. These curves were designed artificially and do not have a physical interpretation in terms of correlated scatterers, but their simplicity and ease of control makes them powerful tools for artistic control of the medium.

Fig. 11. A homogeneous medium with non-exponential, linearly decreasing transmittance rendered with three different rendering algorithms—path tracing, light tracing and bidirectional path tracing—which were modified to support our theory. All three algorithms produce identical images, which shows that our theory produces consistent results in a bidirectional context, despite being non-reciprocal.

Figure 11 shows a similar homogeneous medium with a linearly decreasing, non-exponential transmittance. The same scene is rendered with three different rendering algorithms—path tracing, light tracing and bidirectional path tracing—that were modified to support our theory. All three algorithms produce identical results, which shows that our theory produces consistent results in a bidirectional context.

Figure 1 shows a heterogeneous cloud, rendered with a traditional exponential transmittance, and a long-tailed non-exponential transmittance derived from the Davis and Mineev-Weinstein model. The long tail of the non-exponential transmittance allows light to penetrate deeper into the cloud, which leads to a brighter and softer appearance near the bottom. Simultaneously, the cloud appears denser and more detailed near the surface, giving an overall richer appearance.

Figure 12 shows a cloud rendered with the same fractal noise model over three different colors of noise, but normalized such that all three transmittances have the same mean free path. Even with

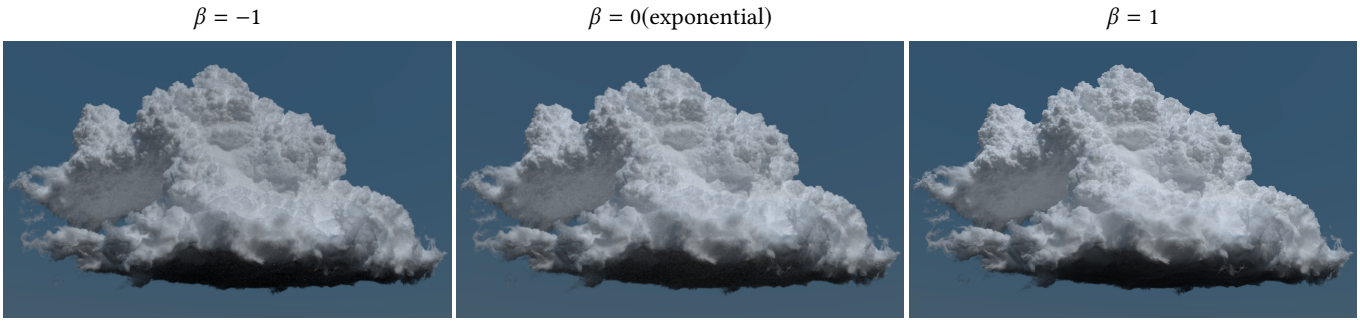

Fig. 12. We compare a cloud rendered with the Davis and Mineev-Weinstein model over three different colors of noise (β), but normalized such that all three transmittances have the same mean free path. Even with this normalization, there are significant appearance changes. This shows that the appearance of the non-exponential transmittance could not be matched with an exponential transmittance of different mean free path.

this normalization, there are significant appearance changes, which shows that the appearance of the non-exponential transmittance could not be matched with an exponential and a scaled heterogeneous density.

Finally, in Figure 13 we compare a heterogeneous cloud rendered using a transmittance derived from fractal noise (bottom two rows) using the Davis and Mineev-Weinstein model with varying parameters (β, C). The fractal noise model allows a range of different appearances and mean free paths. For comparison, we also provide the same cloud rendered using an exponential with varying mean free paths (top row).

We include a comprehensive supplemental material with full-resolution HDR images of all our renderings, including an interactive image viewer for better comparison, Mathematica notebooks of different transmittance functions and additional derivations. We encourage the reader to refer to our supplemental material for a more careful comparison.

8 CONCLUSION

We introduced a new theory of volumetric light transport that allows for media with non-exponential free-flight distributions. Such distributions are the consequence of correlations between scatterers, which can arise from physical processes in e.g. the atmospheric sciences and neutron transport. We showed that the classical RTE conflates the free-flight PDF and the transmittance, which leads to violation of energy conservation when a non-exponential transmittance is used. To resolve these issues, we introduced a new generalization of the RTE that separates the two concepts and allows for an arbitrary free-flight PDF while conserving energy.

We presented a wide range of tools to leverage this newfound flexibility, ranging from simple parametric transmittance curves to powerful mathematical formalisms for Gaussian processes and fractal noise. The latter allowed us to obtain closed-form, ensemble averaged transmittances for scatterers distributed with different colors of noise.

Our theory can be implemented with only minor changes to existing rendering algorithms, and our results demonstrate that this allows for a rich range of volumetric appearances while still allowing for consistent unidirectional and bidirectional transport.

8.1 Limitations and Future Work

There are several limitations to our work that leave ample grounds for future research. Our theory currently assumes that there is a single, globally fixed free-flight PDF. This means that we cannot handle multiple overlapping media with different transmittance functions, even though this could be a useful tool in practice.

Unbiased distance sampling methods, such as Woodcock tracking, implicitly assume the underlying medium to be exponential and cannot be used with our theory. Our implementation therefore has to rely on either expensive (regular tracking) or approximate (raymarching) distance sampling approaches in heterogeneous media. More research is required to adapt efficient, unbiased distance sampling methods for heterogeneous media to our theory.

Although we could obtain a locally optimal distance sampling procedure for paths sampled from the light source, it is unclear how to do the same for paths sampled in the reverse direction. We hope to address this in future work.

An interesting avenue for future research is the synergy between non-exponential transmittance and diffusion theory. In Section 4.1, we took the classical diffusion monopole and interpreted it as a free-flight distribution. Extending this concept to more sophisticated diffusion models could allow for efficient, approximate multi-bounce rendering.

Somewhat surprisingly, the observed transport behavior in a participating medium can be non-exponential even for classical media where the scatterers are independently distributed. Since the weighted average of exponentials is not an exponential, the spectral averaging at the sensor will lead to non-exponential appearance if the medium properties vary across the sensor's spectral response. The ability of our theory to model this non-exponentiality could benefit inverse problems in computer vision and appearance capture, which rely on accurate forward models.

REFERENCES

Michael Ashikhmin and Peter Shirley. 2000. An Anisotropic Phong BRDF Model. *J. Graph. Tools* 5, 2 (Feb. 2000), 25–32. https://doi.org/10.1080/10867651.2000.10487522

Michael Ashikmin, Simon Premože, and Peter Shirley. 2000. A Microfacet-based BRDF Generator. In *Proc. SIGGRAPH*. ACM Press/Addison-Wesley Publishing Co., New York, NY, USA, 65–74. https://doi.org/10.1145/344779.344814

Mahdi M. Bagher, John Snyder, and Derek Nowrouzezahrai. 2016. A Non-Parametric Factor Microfacet Model for Isotropic BRDFs. *ACM Trans. Graph. (Proc. SIGGRAPH)*

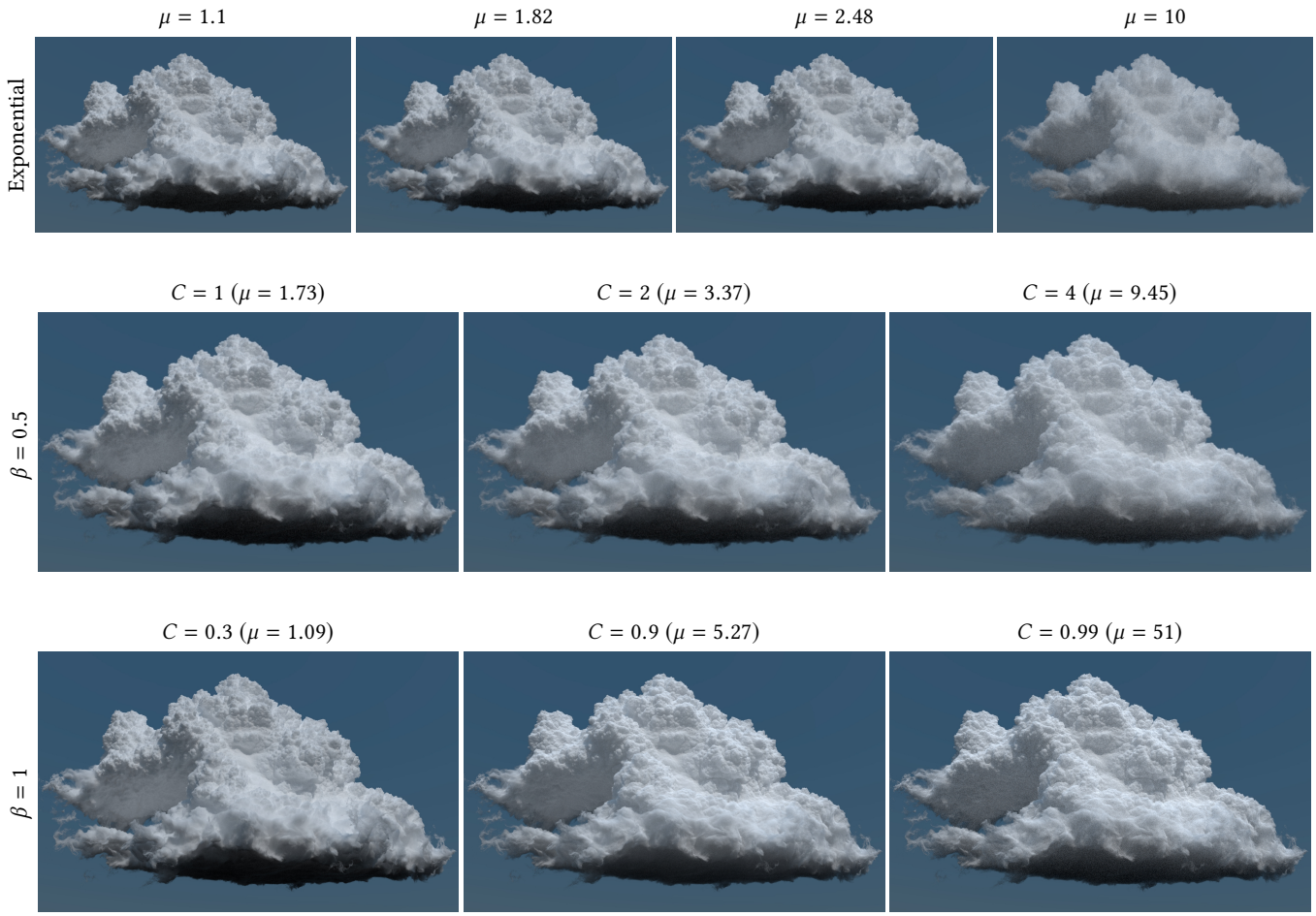

Fig. 13. We compare a heterogeneous cloud rendered using a transmittance derived from fractal noise (bottom two rows) using the Davis and Mineev-Weinstein model with varying parameters (β, C). The fractal noise model allows a range of different appearances and mean free paths. For comparison, we also provide the same cloud rendered using an exponential with varying mean free paths (top row).

35, 5 (July 2016), 159:1–159:16. https://doi.org/10.1145/2907941

Michael F. Barnsley, Robert L. Devaney, Benoit B. Mandelbrot, Heinz-Otto Peitgen, Dietmar Saupe, Richard F. Voss, Yuval Fisher, and Michael McGuire. 1988. *The Science of Fractal Images* (1st ed.). Springer Publishing Company, Incorporated. https://doi.org/10.1007/978-1-4612-3784-6

Benedikt Bitterli. 2018. Tungsten Renderer. (2018). https://github.com/tunabrain/tungsten/.

James F. Blinn. 1977. Models of Light Reflection for Computer Synthesized Pictures. *Proc. SIGGRAPH* 11, 2 (July 1977), 192–198. https://doi.org/10.1145/965141.563893

Anatoli Borovoi. 2002. On the extinction of radiation by a homogeneous but spatially correlated random medium: comment. *J. Opt. Soc. Am. A* 19, 12 (Dec 2002), 2517–2520. https://doi.org/10.1364/JOSAA.19.002517

Antoine Bouthors, Fabrice Neyret, Nelson Max, Eric Bruneton, and Cyril Crassin. 2008. Interactive multiple anisotropic scattering in clouds. In *Proceedings of the Symposium on Interactive 3D Graphics and Games*. ACM, ACM, 173–182. https://doi.org/10.1145/1342250.1342277

S. Chandrasekhar. 1960. *Radiative Transfer*. Dover Publications.

Per H. Christensen and Wojciech Jarosz. 2016. The Path to Path-Traced Movies. *Foundations and Trends in Computer Graphics and Vision* 10, 2 (October 2016), 103–175. https://doi.org/10.1561/0600000073

Robert L. Cook and Kenneth E. Torrance. 1981. A Reflectance Model for Computer Graphics. *Proc. SIGGRAPH* 15, 3 (Aug. 1981), 307–316. https://doi.org/10.1145/965161.806819

Anthony B. Davis and Alexander Marshak. 2004. Photon propagation in heterogeneous optical media with spatial correlations: enhanced mean-free-paths and wider-than-exponential free-path distributions. *Journal of Quantitative Spectroscopy and Radiative Transfer* 84, 1 (2004), 3 – 34. https://doi.org/10.1016/S0022-4073(03)00114-6

Anthony B. Davis, Alexander Marshak, H. Gerber, and Warren J. Wiscombe. 1999. Horizontal structure of marine boundary layer clouds from centimeter to kilometer scales. *Journal of Geophysical Research: Atmospheres* 104, D6 (1999), 6123–6144. https://doi.org/10.1029/1998JD200078

Anthony B. Davis and Mark B. Mineev-Weinstein. 2011. Radiation propagation in random media: From positive to negative correlations in high-frequency fluctuations. *Journal of Quantitative Spectroscopy and Radiative Transfer* 112, 4 (March 2011), 632–645. https://doi.org/10.1016/j.jqsrt.2010.10.001

Anthony B. Davis and Feng Xu. 2014. A Generalized Linear Transport Model for Spatially Correlated Stochastic Media. *Journal of Computational and Theoretical Transport* 43, 1-7 (2014), 474–514. https://doi.org/10.1080/23324309.2014.978083

Eugene d'Eon. 2013. Rigorous asymptotic and moment-preserving diffusion approximations for generalized linear Boltzmann transport in d dimensions. *CoRR* abs/1312.1412 (2013). arXiv:1312.1412 http://arxiv.org/abs/1312.1412

Eugene d'Eon. 2016. *A Hitchhiker's Guide to Multiple Scattering*. Self-published. http://www.eugenedeon.com/project/a-hitchhikers-guide-to-multiple-scattering/

Jonathan Dupuy, Eric Heitz, and Eugene d'Eon. 2016. Additional Progress Towards the Unification of Microfacet and Microflake Theories. In *Proceedings of the Eurographics Symposium on Rendering: Experimental Ideas & Implementations (EGSR '16)*. Eurographics Association, Goslar Germany, Germany, 55–63. https://doi.org/10.2312/sre.20161210

David S. Ebert, F. Kenton Musgrave, Darwyn Peachey, Ken Perlin, and Steven Worley. 2002. *Texturing and Modeling: A Procedural Approach* (3rd ed.). Morgan Kaufmann Publishers Inc., San Francisco, CA, USA.

Julian Fong, Magnus Wrenninge, Christopher Kulla, and Ralf Habel. 2017. Production Volume Rendering: SIGGRAPH 2017 Course. In *ACM SIGGRAPH 2017 Courses (SIGGRAPH '17)*. ACM, New York, NY, USA, Article 2, 79 pages. https://doi.org/10.1145/3084873.3084907

Diego Gutierrez, Francisco Seron, Adolfo Muñoz, and Oscar Anson. 2008. Visualizing Underwater Ocean Optics. *Computer Graphics Forum (Proc. Eurographics)* 27, 2 (2008), 547–556.

Eric Heitz, Jonathan Dupuy, Cyril Crassin, and Carsten Dachsbacher. 2015. The SGGX Microflake Distribution. *ACM Trans. Graph.* 34, 4 (July 2015), 48:1–48:11.

Wenzel Jakob, Adam Arbree, Jonathan T. Moon, Kavita Bala, and Steve Marschner. 2010. A Radiative Transfer Framework for Rendering Materials with Anisotropic Structure. *ACM Trans. Graph.* 29, 4, Article 53 (July 2010), 13 pages. https://doi.org/10.1145/1778765.1778790

Adrian Jarabo and Victor Arellano. 2018. Bidirectional Rendering of Vector Light Transport. *Computer Graphics Forum* (2018), n/a–n/a. https://doi.org/10.1111/cgf.13314 awaiting publication.

A. Keller, L. Fascione, M. Fajardo, I. Georgiev, P. Christensen, J. Hanika, C. Eisenacher, and G. Nichols. 2015. The Path Tracing Revolution in the Movie Industry. In *ACM SIGGRAPH 2015 Courses (SIGGRAPH '15)*. ACM, New York, NY, USA, Article 24, 7 pages. https://doi.org/10.1145/2776880.2792699

Alexander B. Kostinski. 2001. On the extinction of radiation by a homogeneous but spatially correlated random medium. *J. Opt. Soc. Am. A* 18, 8 (Aug 2001), 1929–1933. https://doi.org/10.1364/JOSAA.18.001929

A. B. Kostinski and A. R. Jameson. 2000. On the Spatial Distribution of Cloud Particles. *Journal of the Atmospheric Sciences* 57, 7 (2000), 901–915.

Edward W. Larsen and Richard Vasques. 2011. A generalized linear Boltzmann equation for non-classical particle transport. *Journal of Quantitative Spectroscopy and Radiative Transfer* 112, 4 (2011), 619 – 631.

Benoit B. Mandelbrot and John W. Van Ness. 1968. Fractional Brownian Motions, Fractional Noises and Applications. *SIAM Rev.* 10, 4 (1968), 422–437. https://doi.org/10.1137/1010093

Wojciech Matusik, Hanspeter Pfister, Matt Brand, and Leonard McMillan. 2003. A Data-Driven Reflectance Model. *ACM Trans. Graph. (Proc. SIGGRAPH)* 22, 3 (July 2003), 759–769. https://doi.org/10.1145/882262.882343

Johannes Meng, Marios Papas, Ralf Habel, Carsten Dachsbacher, Steve Marschner, Markus Gross, and Wojciech Jarosz. 2015. Multi-scale Modeling and Rendering of Granular Materials. *ACM Trans. Graph.* 34, 4, Article 49 (July 2015), 13 pages. https://doi.org/10.1145/2766949

Jonathan T. Moon, Bruce Walter, and Steve Marschner. 2008. Efficient Multiple Scattering in Hair Using Spherical Harmonics. *ACM Trans. Graph. (Proc. SIGGRAPH)* 27, 3, Article 31 (Aug. 2008), 7 pages. https://doi.org/10.1145/1360612.1360630

Jonathan T. Moon, Bruce Walter, and Stephen R. Marschner. 2007. Rendering Discrete Random Media Using Precomputed Scattering Solutions. In *Rendering Techniques (Proc. EGSR)*. 231–242.

Thomas Müller, Marios Papas, Markus Gross, Wojciech Jarosz, and Jan Novák. 2016. Efficient Rendering of Heterogeneous Polydisperse Granular Media. *ACM Trans. Graph.* 35, 6, Article 168 (Nov. 2016), 14 pages. https://doi.org/10.1145/2980179.2982429

Derek Nowrouzezahrai, Jared Johnson, Andrew Selle, Dylan Lacewell, Michael Kaschalk, and Wojciech Jarosz. 2011. A Programmable System for Artistic Volumetric Lighting. *ACM Trans. Graph. (Proc. SIGGRAPH)* 30, 4, Article 29 (Aug. 2011). https://doi.org/10.1145/2010324.1964924

Matt Pharr, Wenzel Jakob, and Greg Humphreys. 2016. *Physically Based Rendering: From Theory to Implementation* (3rd ed.). Morgan Kaufmann Publishers Inc., San Francisco, CA, USA.

Bui Tuong Phong. 1975. Illumination for Computer Generated Pictures. *Commun. ACM* 18, 6 (June 1975), 311–317. https://doi.org/10.1145/360825.360839

Raymond A Shaw, Alexander B Kostinski, and Daniel D Lanterman. 2002. Super-exponential extinction of radiation in a negatively correlated random medium. *Journal of Quantitative Spectroscopy and Radiative Transfer* 75, 1 (2002), 13 – 20. https://doi.org/10.1016/S0022-4073(01)00287-4

Richard Vasques and Edward W. Larsen. 2014a. Non-classical particle transport with angular-dependent path-length distributions. I: Theory. *Annals of Nuclear Energy* 70, Supplement C (2014), 292 – 300. https://doi.org/10.1016/j.anucene.2013.12.021

Richard Vasques and Edward W. Larsen. 2014b. Non-classical particle transport with angular-dependent path-length distributions. II: Application to pebble bed reactor cores. *Annals of Nuclear Energy* 70, Supplement C (2014), 301 – 311. https://doi.org/10.1016/j.anucene.2013.12.020

Magnus Wrenninge, Chris Kulla, and Viktor Lundqvist. 2013. Oz: The Great and Volumetric. In *ACM SIGGRAPH 2013 Talks (SIGGRAPH '13)*. ACM, New York, NY, USA, Article 46, 1 pages. https://doi.org/10.1145/2504459.2504518

Magnus Wrenninge, Ryusuke Villemin, and Christophe Hery. 2017. *Path Traced Subsurface Scattering using Anisotropic Phase Functions and Non-Exponential Free Flights*. Technical Report.

Magnus Wrenninge, Nafees Bin Zafar, Ollie Harding, Gavin Graham, Jerry Tessendorf, Victor Grant, Andrew Clinton, and Antoine Bouthors. 2011. Production Volume Rendering 2: Systems. In *ACM SIGGRAPH 2011 Courses*. ACM, New York, NY, USA.